The cold gaseous halo of NGC 891

Tom Oosterloo

Netherlands Foundation for Research in Astronomy, Dwingeloo, The Netherlands
Kapteyn Institute, Groningen, The Netherlands

oosterloo@astron.nl

Filippo Fraternali

Department of Astronomy, University of Bologna, Italy

and

Renzo Sancisi

INAF - Osservatorio di Bologna, Italy
Kapteyn Institute, Groningen, The Netherlands

ABSTRACT

We present H I observations of the edge-on galaxy NGC 891. These are among the deepest ever performed on an external galaxy. They reveal a huge gaseous halo, much more extended than seen previously and containing almost 30% of the H I. This H I halo shows structures on various scales. On one side, there is a filament extending (in projection) up to 22 kpc vertically from the disk. Small ($M_{\rm HI} \gtrsim 10^6\ M_\odot$) halo clouds, some with forbidden (apparently counter-rotating) velocities, are also detected. The overall kinematics of the halo gas is characterized by differential rotation lagging with respect to that of the disk. The lag, more pronounced at small radii, increases with height from the plane. There is evidence that a significant fraction of the halo is due to a galactic fountain. Accretion from intergalactic space may also play a role in building up the halo and providing low angular momentum material needed to account for the observed rotation lag. The long H I filament and the counter-rotating clouds may be direct evidence of such accretion.

Subject headings: galaxies: halos — galaxies: kinematics and dynamics — galaxies: structure — galaxies: individual (NGC 891)

1. Introduction

Recent deep observations of the neutral hydrogen of several nearby spiral galaxies indicate that up to about 15% of the neutral hydrogen of a spiral galaxy is located in the halo. The best examples are: NGC 891 (Swaters, Sancisi, & van der Hulst 1997); NGC 2403 (Schaap, Sancisi & Swaters 2000; Fraternali et al. 2001); NGC 4559 (Barbieri et al. 2005); M31 (Westmeier, Braun, & Thilker 2005); UGC 7321 (Matthews & Wood 2003); NGC 253 (Boomsma et al. 2005b); NGC 5775 (Lee et al. 2001) and NGC 6946 (Boomsma et al. 2005a; Boomsma 2007). Overall, the kinematics of the halo gas is quite regular. The main motion is differential rotation parallel to the plane. However, the rotation velocities in the halo are lower than in the disk (Swaters, Sancisi, & van der Hulst 1997; Fraternali et al. 2002). In some cases a small overall radial inflow is found superposed on the rotation (Fraternali et al. 2001). On small scales strong vertical motions from and towards the disk are also observed (Boomsma et al. 2005a; Boomsma 2007). Halo gas is also detected in Hα (e.g. Hoopes, Walterbos & Rand 1999; Rossa & Dettmar 2003), with kinematics similar to that of the neutral gas (Rand 2000; Tüllmann et al. 2000; Fraternali, Oosterloo & Sancisi 2004; Heald et al. 2006a, 2007; Kamphuis et al. 2007), and in X-rays (e.g. Strickland et al. 2004).

The origin of the gaseous halos is still a matter of debate. The *galactic fountain* mechanism (Shapiro & Field 1976) has received most attention to date. In this scheme, gas is pushed into the halo by stellar winds and SN explosions, mostly in the **hot** ionized phase. This gas travels through the halo, eventually cools to neutral and falls back to the disk (Bregman 1980). **There is strong observational evidence supporting the fountain mechanism, such as the close correlation between the distribution of** Hα **and the high-velocity gas found in NGC 6946 (Boomsma 2007), as well as that the star formation rate appears to correlate with the luminosity of the X-ray halo (Tüllmann et al. 2006b) and with the radio continuum emission of the halo (Dahlem et al. 2006)**. However, the sample of galaxies studied so far is still too small to be able to make any statement on whether flows related to star formation are the dominant mechanism or not **in particular for the neutral halos**. Furthermore, **there are indications that an ionized halo only builds up if the star formation rate is above a critical value (Tüllmann et al. 2006b) which may pose a problem for the H I halo detected in the super-thin LSB UGC 7321, a galaxy with a low star formation rate (Matthews & Wood 2003)**. The main problem for the fountain mechanism comes, however, from the study of the kinematics. Simple (i.e. so-called *ballistic*) models have been unable to reproduce the kinematics of the ionized gas (Collins, Benjamin & Rand 2002; Heald et al. 2006a). Recently, Fraternali & Binney (2006) have shown that also the kinematics of the neutral halo gas cannot be explained by "pure" ballistic galactic fountains. This suggests that other effects, such as the interaction with a pre-existing hot halo or the accretion

from intergalactic space, must play an important role. There have also been attempts to model the extra-planar gas as a stationary medium in hydrostatic equilibrium (Benjamin 2002; Barnabè et al. 2005), or as a cooling flow accretion in a CDM context (Kaufmann et al. 2006), but none of these models is able to reproduce the observations completely. It is possible that the halo gas is the result of complex phenomena involving both internal and external processes.

Understanding the origin and nature of the gaseous halos surrounding spiral galaxies is important for several reasons. First, the halo is the region where material can be exchanged between different parts of the galaxy and this circulation of gas is fundamental for the galactic life-cycle. Secondly, galactic halos are the interface between the galaxy, which is visible and well studied, and the Intergalactic Medium (IGM), the content and properties of which remain largely unknown. CDM cosmological models predict that most of the baryonic material is currently in the IGM (e.g. White & Frenk 1991; Sommer-Larsen 2006). The discovery of the halo gas may provide a new and efficient way to probe the IGM by studying the exchange of material between galaxies and their environment.

We believe that the halo gas observed in external galaxies is the analogue of the Intermediate- and High-Velocity Clouds (IVCs and HVCs) of the Milky Way (Wakker & van Woerden 1997). The cloud complexes with anomalous velocities found in galaxies like NGC 2403 (Fraternali et al. 2002) have similar masses and velocity deviations with respect to the disk as the largest galactic HVCs for which the distances are known (e.g. complex A, Wakker 2001). The total gas mass of the HVCs, if located in the halo at distances up to a few tens of kpc, would be of the order of 10^8 $M_\odot$, similar to that of the H I found in the halos of external galaxies (e.g. NGC 891, Swaters, Sancisi, & van der Hulst 1997; NGC 2403, Fraternali et al. 2002). It is therefore interesting to note that some of the HVCs, in particular complex C, have been found to have a low metallicity ($Z \sim 0.1 - 0.3$ $Z_\odot$; Tripp et al. 2003). This may indicate that some of the HVCs are accretion from the surrounding IGM of "unprocessed" material onto the disk of our Galaxy. Such accretion may be necessary to explain the evolution of disk galaxies (Naab & Ostriker 2006). Accretion onto disk galaxies may also occur as the merging of small, gas-rich satellites (van der Hulst & Sancisi 1988, 2005). Recently, a search has been carried out for the two largest members of the Local Group other than the Milky Way: M31 and M33 (Westmeier, Braun, & Thilker 2005) and a population of high-velocity clouds at large distances from these galaxies (about 50 kpc from M31, Thilker et al. (2004)) has been found. These clouds have typical masses of a few times 10^5 $M_\odot$. Most of them are thought to be remnants of the accretion of small companion galaxies, although a small fraction might be primordial gas clouds (Westmeier, Braun, & Thilker 2005).

In this paper, we present very deep H I observations of the nearby edge-on spiral galaxy NGC 891 obtained with the upgraded Westerbork Synthesis Radio Telescope (WSRT). NGC 891 is an Sb/SBb galaxy, one of the best studied nearby edge-on galaxies. The disk of NGC 891 shows intensive star formation at a rate of $\sim 3.8\ M_\odot\,\mathrm{yr}^{-1}$ (Popescu et al. 2004). The halo region has been studied at various wavelengths and shows a variety of components from radio continuum emission (e.g. Allen, Sancisi & Baldwin 1978) to hot diffuse gas (e.g. Bregman & Pildis 1994). NGC 891 is considered to be very similar to the Milky Way **with regard to mass and stellar components** (van der Kruit 1984) **although it has a higher star formation rate and significantly stronger radio continuum emission**. A summary of its physical parameters is given in Table 1.

In the past, NGC 891 has been studied in H I several times with ever increasing sensitivity (e.g. Sancisi & Allen 1979; Rupen 1991; Swaters, Sancisi, & van der Hulst 1997). The first indication of extra-planar material had been reported already by Sancisi & Allen (1979), but their favored explanation was that of a flaring outer disk. Almost two decades later Becquaert & Combes (1997) proposed a different interpretation in terms of a warp of the H I disk along the line of sight. Finally, more sensitive WSRT observations of NGC 891 revealed a much more extended extra-planar component (Swaters, Sancisi, & van der Hulst 1997) and a careful modeling of the full data cube showed that the most likely explanation was that of an extended halo component rotating more slowly than the disk. Here we report the results of H I observations that are a factor 5 more sensitive than those of Swaters, Sancisi, & van der Hulst (1997). These observations reveal that the gaseous halo is much more extended than showed by the previous data.

2. Observations

The present observations were obtained with the Westerbork Synthesis Radio Telescope in the period August - December 2002. In total, 20 complete 12-hour observations were performed, using five of the standard array configurations. The combination of these different configurations gives a regular sampling of the uv plane from the shortest spacing of 36 m to the longest baseline of 2754 m, with an interval of 36 m. Care was taken not to use data affected by solar interference that might have compromised the detection of faint, extended emission from the halo. The effective integration time corresponds to that of 17 complete 12-hour observations. The observing bandwidth is 10 MHz (corresponding to about 2000 km sec^{-1}), using 1024 channels (with 2 independent polarizations). An overview of the observational parameters is given in table 2. The data processing was done using the MIRIAD package (Sault Teuben & Wright 1995). Before and after each 12-hr observation a

standard calibrator was observed (J2052+365 and 3C147) from which the spectral response of the telescope was determined. As is standard practice with the WSRT, during each 12-hr track no additional (phase) calibrators were observed to monitor the time variation of system properties. Instead, the large bandwidth allows to determine these by self-calibration of the continuum image made from the line-free channels of the data. This self-calibration was done using a model of the continuum emission based on the combination of all observations. An advantage of this approach is that it also gives an excellent removal of the continuum sources in the line images, as well as a well-calibrated continuum image (see Sec. 3.4).

Three datacubes were made with three spatial resolutions $23.4'' \times 16.0'', 33.2'' \times 23.9''$ and $69.6'' \times 58.9''$ (see Table 3). The line data were combined and gridded into cubes of 224 channels 8.2 km sec^{-1} wide to which additional Hanning smoothing was applied. This results in a velocity resolution of 16.4 km sec^{-1}. **As always with radio observations, the highest-resolution data set has the lowest noise level (0.09 mJy beam^{-1}), the 30- and 60-arcsec data sets have noise levels of 0.10 and 0.12 mJy beam^{-1} respectively** . The 3-σ detection limits over one resolution element in the three datacubes are 1.3×10^{19} cm^{-2}, 6.8×10^{18} cm^{-2} and 1.6×10^{18} cm^{-2}. The datacubes were cleaned using the Clark algorithm. In an iterative procedure, regions with line emission were identified by smoothing the data to twice the spatial resolution and selecting a clip level by eye to define the mask where to clean the data. This procedure was repeated until convergence was achieved.

The H I flux integral is $1.92 \cdot 10^2$ Jy km sec^{-1} corresponding to a H I mass of $4.1 \cdot 10^9$ $M_\odot$[1]. The mass derived here is 10% more than found by Sancisi & Allen (1979) and by Rupen (1991), but the same as derived by Braun, Thilker & Walterbos (2003).

3. Observed properties

3.1. Density map

In Fig. 1 (right panel) we show the total H I image for NGC 891 at 30″ resolution. This image was obtained in the standard way by smoothing the datacube to a resolution of 40″ and using this smoothed cube to create a mask to be applied to the original cube. The mask was produced by blanking emission below +3 r.m.s. noise in the smoothed cube. To illustrate the effects of the improvement in sensitivity of almost two orders of magnitude, in Fig. 1 we also give the H I density distribution as published in two previous studies of NGC

[1]we assume a distance to NGC 891 of 9.5 Mpc, (van der Kruit 1981); 1′ corresponds to 2.76 kpc

891 (Sancisi & Allen 1979; Swaters, Sancisi, & van der Hulst 1997). One feature immediately clear from Fig. 1 is that, despite the large improvement in sensitivity, the radial extent of the H I disk has *not* become significantly larger and that *in the plane*, the new observations do not reveal any basically new features (see below).

However, in the vertical direction the situation is dramatically different and in the new observations the H I extends much farther above the plane. The extra-planar emission in NGC 891, barely visible in the data of Sancisi & Allen (1979) and detected up to 5 kpc in Swaters, Sancisi, & van der Hulst (1997), is now detected up to a projected distance of **more than 10 kpc from the plane everywhere and more than 20 kpc in a filamentary structure in the NW**. Integrating the flux density located above and below 1 kpc from the plane, we find that the H I in the halo represents 29% (1.2×10^9 $M_\odot$) of the total H I content of NGC 891. As one can see from the lowest contours, the difference in sensitivity between our total H I map and that of Swaters, Sancisi, & van der Hulst (1997) is about a factor 5. The H I observations presented here are among the deepest ever obtained for an external spiral galaxy. It is therefore quite possible that also other galaxies, if observed with comparable high sensitivity, would show similar extended extra-planar emission and gaseous halos may be a common feature among spiral galaxies.

The vertical extent of the H I layer is illustrated in Fig. 2 where we plot the normalised average H I column density, based on the 30 arcsecond dataset, for the four quadrants of the galaxy. In the NE, SE and SW quadrants the H I halo extends out to about $5'$ (14 kpc) while in the NW quadrant it extends even further out to about $8'$ ($\sim$22 kpc). The density profiles in the NE, SE and SW quadrants are very similar and can be modelled quite well with an exponential profile with scaleheight of 50 arcsec (2.2 kpc). In the NW quadrant the density distribution seems to follow the same trend out to about $3'$ (8.3 kpc) after which it becomes flatter. This larger extent in the NW quadrant corresponds to a large filament extending out to more than 20 kpc from the disk (see Fig. 1).

Around the NW filament a crowd of high-latitude clouds are observed (Figs. 4 and 16), which are probably associated with the filament itself. However, individual gas clouds are also observed at large radii and at very anomalous velocities (with large deviations from rotation). The middle panels of Fig. 16 show two of these clouds at "apparently" counter-rotating velocities. The first is in the N-W quadrant at velocities that differ by about 100 km sec^{-1} from the velocity of the halo at that position. This cloud is probably located in the outskirts of the halo, otherwise the drag force of the halo would invert its motion very quickly. The second cloud is detected (Fig. 16, middle right) at a projected distance of about 28 kpc from the center of the galaxy. These clouds have masses

of $M_{\rm HI} \sim 1 - 3 \times 10^6\ M_\odot$**.**

As stated above, the new data do not reveal significant new features at large radii in the plane of the disk. As the earlier data showed, the H I disk of NGC 891 is not symmetric, being more extended on the South-West side. The fall-off and disappearance of the H I disk on the northern side of NGC 891, approximately coincident with the end of the stellar disk, and the large southern extension, confirm the picture of lopsidedness already known from previous observations and discussed by Baldwin, Lynden-Bell & Sancisi (1980). However, the fact that, despite the large improvement in sensitivity, NGC 891 does not grow in radius but does grow substantially in the vertical direction, poses an interesting question. The presence and the origin of outer cut-offs of H I disks have been a matter of debate in the past years. One of the favored explanations for their origin has been the effect of the extragalactic radiation field (Maloney 1993). In the case of NGC 891 such an explanation would immediately encounter a serious objection: why would the H I be ionized by a presumably isotropic radiation field in the plane of the galaxy (and account for the northern truncation) and apparently not be affected at all in the low-density halo regions? Unless the time scales for the disk and for the halo gas and for their respective ionizations are significantly different, it seems more likely that the disappearance of H I on the northern side of NGC 891 simply marks the outer boundary of the gaseous disk.

3.2. Kinematics

The kinematics of the H I gas is shown by the position-velocity (p-V) diagrams parallel and perpendicular to the disk (Figs. 3 and 4). In these diagrams, the high-resolution data are shown with thin contours and the grayscale, while the thick contours show the low-resolution ($60''$) data at a 3-σ level. The low resolution is intended to outline the full extent of the faint emission. The upper plot in Fig. 3 shows the distribution along the major axis (i.e. in the plane) of NGC 891. The rotation curve is shown by the squares and crosses in Fig. 5. This has been derived by tracing the "envelope', as already done and described by Sancisi & Allen (1979), and using a gas velocity dispersion of 8 km/s. This method is also used by Fraternali (2007, in preparation) to derive the rotation curves for the halo gas of NGC 891 at various distances from the plane. As already mentioned, the disk of NGC 891 is lopsided, being more radially extended on the receding S-W side. The rotation in the plane is characterized by an inner peak produced by a fast-rotating inner ring or by a bar (Garcia-Burillo & Guelin 1995). This feature is symmetric with respect to the center and also with respect to the systemic velocity. Beyond this, the disk is clearly dominated by differential rotation showing a roughly flat rotation curve out to a distance of about $6'$ ($\sim$17 kpc) from the center (Fig.

5). The receding side extends further out with an apparent decrease in rotational velocity. However, we do not know the azimuthal location of this extension in the plane of NGC 891. If this is not along the line of nodes, the decrease in rotational velocity is only apparent and due to projection effects. Note, however, that this extension probably represents a large fraction of the outer disk as it can be seen in the p-V diagram of Fig. 5 on the entire receding side at projected distances from $0'$ to $11'$ and on the velocity side closer to systemic.

Above and below the plane of the disk (lower panels in Fig. 3), the shape of the p-V diagrams changes dramatically. First, the fast-rotating inner component quickly disappears, indicating that it is confined to the inner thin disk. Moreover, the overall shape of the diagram changes from that of a typical differentially rotating disk to that of solid-body rotation. In particular, the two diagrams at $z = \pm 3'$ from the plane clearly show the pattern of a slow solid-body rotator. These features are a first indication for a slow rotation of the gas above the plane with respect to that in the disk.

The p-V diagrams in Fig. 4 show the vertical density-velocity structure of NGC 891. The shape of these plots is generally triangular with the vertex located at the highest rotation velocity (in the plane). This shape was already noted by Sancisi & Allen (1979) in their Figure 7, showing the H I emission on the receding and the approaching sides. At increasing distances upward and downward from the plane, the emission tends to disappear from the high rotation velocity side and to be restricted closer and closer to the systemic velocity ($V_{\rm sys}$ = 528 km sec^{-1}). This is particularly clear for the emission at very high latitudes. The p-V diagrams at distances from $R = -1'$ to $R = -3'$ (i.e. at $1'$ and $3'$ from the center of the galaxy on the N-E side) show emission at low levels up to about $8'$ ($\sim$22 kpc) and concentrated around the systemic velocity of NGC 891. This is the filament visible (Fig. 1) on the NW side of the galaxy.

The p-V diagrams also show that, if one compares the halo gas in the different quadrants, the kinematics of this gas is quite symmetric up to heights of about $3'$ ($\sim$8 kpc). Beyond this, significant differences exist between the quadrants. This symmetric kinematics in the lower halo could indicate that the gaseous halo in this region is in a equilibrium situation.

A synoptic view of the kinematical structure of the H I gas in the vertical direction (from the disk to the halo region) is shown in Fig. 6 where the thickness of the H I (measured as the first moment of the z-distribution) is given as a function of position along the major axis and radial velocity. At the high velocity side (close to rotation) the z-distribution is much thinner than at the lower rotational velocity side as also seen in Fig. 4.

3.3. UGC 1807

The present observations show also UGC 1807, a small, gas-rich companion located at a projected distance of about 30′ ($\sim$ 80 kpc) from NGC 891 (Fig. 7) (not discussed in previous papers on NGC 891). In the optical, UGC 1807 appears as a LSB galaxy oriented almost face-on. Our H I data show a regular distribution of H I with a symmetric velocity field (Fig. 7). The outer radius of the H I disk is 4 kpc and the total H I mass corrected for the primary beam attenuation is 4.5×10^8 $M_\odot$. We note that at the position of UGC 1807 this correction is quite large, about a factor 6.

The kinematic parameters of UGC 1807 have been derived with a tilted-ring fit of the velocity field. We found a systemic velocity of 627 km sec^{-1}, 100 km sec^{-1} larger than that of NGC 891, and an inclination of about 15°$\pm$ 5°. The rotation curve (Fig. 7) is very regular and shows a slow rising in the inner regions up to a rotation velocity of about 100 km sec^{-1} at the last measured point. However, because of the low inclination and its large uncertainty, the amplitude of the rotation curve is very uncertain: it can be as low as 70 km sec^{-1} or as high as 140 km sec^{-1}. Using 100 km sec^{-1} and the measured outer radius, we find for UGC 1807 a total mass of 9×10^9 $M_\odot$.

3.4. Radio Continuum

Thanks to the broad band and the long integration time of the present observations we have been able to construct a very deep radio continuum image (Fig. 8), similar in quality to the 21-cm continuum image published by Dahlem, Dettmar & Hummel (1994). The spatial resolution is 17×12 arcsec, the RMS noise is 23 μJy beam^{-1}. Our data do not contain, however, the information on the polarization of the radio emission. In Fig. 9 we show the normalized vertical brightness distribution of the radio continuum halo in the four quadrants of NGC 891. As was found by Dahlem, Dettmar & Hummel (1994), the vertical brightness distribution of the radio continuum closely follows an exponential profile with a scaleheight of 25 arcsec (corresponding to 1.15 kpc) in the NE, SE and SW quadrants and a bit larger (1.3 kpc) in the NW quadrant. In the SW quadrant the radio continuum halo seems to be somewhat more extended. As in the earlier data on NGC 891, there is also a strong N-S asymmetry of the continuum emission in the disk. Dahlem et al. argue, based on the similarity in the distribution of the Hα emission and the radio continuum, that both are the result of outflows from the disk driven by star formation. In Fig. 9 we also indicate the vertical distribution of the Hα emission of the halo, as determined by Rand & Heald (priv. comm.).

4. Models

Here we investigate the structure and kinematics of the extra-planar **H I** emission in NGC 891 by constructing model datacubes and comparing these with the observations. We first consider, following Swaters, Sancisi, & van der Hulst (1997), basic models (Section 4.1) in which the extra-planar emission is produced by a **strong** warp, a flare and a co-rotating thick disk. All these models are easily ruled out by the comparison with the data. Then, in Section 4.2, we consider more sophisticated models made of two components (disk + halo) with different kinematics.

4.1. Basic models

We build model datacubes using a modified version of the GIPSY (van der Hulst et al. 1992) program GALMOD. This program assumes axi-symmetry and an H I layer made of concentric rings. For each ring we define the H I column density, the thickness of the layer and the geometrical and kinematic parameters. The H I disk of NGC 891 is not symmetric, being more extended on the SW (receding) side of the galaxy. In order to avoid the complications arising from this lopsidedness we construct the models only for the NE (approaching) side of the galaxy.

We start with a thin disk model. The H I radial density distribution in the plane of the disk is derived by considering only the NE side of the galaxy and the region within $|z| < 30''$. The result is plotted in Fig. 10. We approximate the observed distribution with an exponential law at large radii and a depression in the inner regions as described by:

$$\Sigma(R) = \Sigma_0 \left(1 + \frac{R}{R_*}\right)^{\alpha} \exp\left(-R/R_*\right), \tag{1}$$

where Σ_0 is the central surface density, α is an exponent defining the tapering towards the center and R_* is a scale radius such that the peak of the distribution is located at $R = R_*(\alpha - 1)$. The parameters of the fit shown in Fig. 10 are $\Sigma_0 = 6.2 \times 10^{-4}\ M_\odot\,\mathrm{pc}^{-2}$, $\alpha = 7.8$ and $R_* = 1.2$ kpc. In the inner regions of the galaxy ($R \lesssim 3$ kpc) this model fails to reproduce the inner ring that is clearly visible in Fig. 5. To reproduce also this inner ring, we add an extra exponential component to our model. **The parameters of this component are** $\Sigma_0 = 6.3\ M_\odot\,\mathrm{pc}^{-2}$ **and** $R_* = 1.2$ **kpc**. The approaching and receding rotation curves in the disk of NGC 891 are shown in Fig. 5. In our models, we use the curve derived for the N-E (approaching) side of the galaxy and we assume a velocity dispersion $\sigma_{\mathrm{gas}} = 8$ km sec^{-1}.

NGC 891 has a mild warping of the outer disk, as can be seen in the top-right plot in Fig. 11. **In all models, we have included this mild warp** by varying the inclination

and position angles of the rings beyond $R = 13$ kpc. The warping angles that fit the data are quite small (1.5° in p.a. and 4° in inclination). The inclination angle of the inner disk is taken to be 90°. The vertical distribution has been modeled with an exponential profile with scaleheight $h_{\rm disk} = 0.2$ kpc.

Fig. 11 (leftmost column) shows the best fit thin disk model for NGC 891. The rightmost column shows the data channel maps at full resolution. An important property of the data is that the *apparent* vertical thickness increases from very thin in the $v_{\rm hel} = 292$ km sec^{-1}channel (corresponding to the extreme rotation velocity) to a broad vertical distribution in the bottom channel (close to the systemic velocity, $v_{\rm sys} = 528$ km sec^{-1}). This is a major constraint for all our models as it indicates that there is no halo gas with rotation velocities as high as those of the gas in the disk. Clearly the thin disk model only reproduces the top channel at $v_{\rm hel} = 292$ km sec^{-1}. The gas visible in this channel is likely to be at the line of nodes and its thickness is a measure of the intrinsic thickness of the thin disk. However, because of the insufficient resolution (HPBW = $19'' \simeq 0.9$ kpc in the vertical direction) this channel gives only an upper limit to the thickness of the thin disk (see below).

The second column of Fig. 11 shows the effect of a strong warp along the line of sight **in addition to the mild warp described above**. Such a **strong** warp model has been proposed by Becquaert & Combes (1997) to explain the extra-planar emission observed in NGC 891 with the VLA (Rupen 1991), in contrast with the model of a thick, lagging layer favored by Swaters, Sancisi, & van der Hulst (1997). In the present model we have introduced a linear change in the inclination of the outer rings (beyond $R = 13$ kpc) that reaches a tilt of 25° in the outermost ring with respect to the inner parts (i = 90°). This model comes close for the top and the bottom channels of Fig. 11 but totally fails to reproduce the middle ones. The characteristic feature of any line-of-sight warp model is the "butterfly" opening visible in the middle channels (around $v_{\rm hel} = 366.2$ km sec^{-1}) (see also Gentile et al. 2003). Such a pattern is totally absent in the present data and, therefore, we can rule out that the extra-planar emission in NGC 891 is produced by a line-of-sight warp.

The middle column of Fig. 11 shows the effect of a large flaring of the H I layer. In this model, the thickness of the H I layer in the inner regions is as small as in the thin-disk model ($h_{\rm disk} \simeq 0.2$ kpc) but it increases outwards and reaches $h_{\rm disk} \simeq 3$ kpc in the outer rings. Such an unrealistically large value is necessary to produce the emission observed at high latitudes. This model generates some channel maps fairly similar to those observed (e.g. at $v_{\rm hel} = 366.2$ km sec^{-1}), but it completely fails to reproduce the thin structure in the top channel maps. This is because in the model the gas in the outer flare rotates as fast as the gas in the plane. Also this model, therefore, can be ruled out. As already mentioned above, from the thin structure observed at the highest rotational velocities (top Fig. 11) it is

possible to derive an upper limit to the thickness of the thin disk and to set an upper limit to its flaring. We find that the inner scaleheight of the disk is less than $h_{\rm disk} < 0.3$ kpc, while in its outer regions the disk can flare up to at most $h_{\rm disk} \sim 0.5$ kpc.

We now consider models made of two components: 1) a thin disk (like that in the leftmost column in Fig. 11) and 2) a thicker layer or halo. For the vertical gas distribution of the latter we use a density profile described by the following empirical function:

$$\zeta(z) = \zeta_0 \frac{\sinh(z/h_{\rm halo})}{\cosh(z/h_{\rm halo})^2} \tag{2}$$

where z is the vertical coordinate, ζ_0 is the surface density in the plane and $h_{\rm halo}$ is the halo scaleheight. With this formulation, the vertical density of the thick layer is zero in the plane, then rises reaching its maximum at $z = 0.88 h_{\rm halo}$ and declines nearly exponentially further out. The half width at half maximum (HWHM) of this distribution (defined as the z where $\zeta(z) = \zeta(0.88 h_{\rm halo}/2)$ is at $z = 2 h_{\rm halo}$. Between disk and halo there is a gradual transition. In this way the spatial coexistence between the two components is minimized: the halo takes over when the disk is fading out.

In order to model the gas density in the halo, we have extracted and deprojected the radial distributions at various heights. The left panel of Fig. 12 shows (squares) two of these deprojected radial distributions at$z = 2.8$ **and** $z = 5.6$ **kpc (average of the NE and NW quadrants). The shapes of these distributions change with the height from the plane: as the distance from the plane increases, the radial distribution becomes flatter and less concentrated to the center (cf. Fig. 10). We have fitted the data with the function:**

$$\rho_{\rm halo}(R,z) = \Sigma(R) \frac{\zeta(z; h_{\rm halo}(R))}{\zeta_0} \tag{3}$$

where $\Sigma(R)$ **and** $\zeta(z; h_{\rm halo})$ **are given by equations 1 and 2 but the scaleheight** $h_{\rm halo}$ **varies with** R**. Fig. 12 (right) shows the fitted values (squares) of** $h_{\rm halo}$ **as a function of** R **and a power law fit (solid line). With this parametrization the scaleheight of the halo varies from** $h_{\rm halo} = 1.25$ **kpc (HWHM=** 2.5 **kpc) in the central regions to** $h_{\rm halo} \sim 2.5$ **kpc (HWHM**~ 5 **kpc) in the outer parts. The other parameters of the fit are:** $\Sigma_0 = 1.4 \times 10^{-1}\ M_\odot\,{\rm pc}^{-2}$**,** $\alpha = 4.5$**,** $R_* = 1.9$ **kpc. The final result is shown (lines) in the left panel of Fig. 12 (at** $z = 2.8$ **and** $z = 5.6$ **kpc from the plane).**

The forth column in Fig. 11 shows a two-component model in which the halo co-rotates with the disk. The mass of the halo component is $M_{\rm halo} = 1.25 \times 10^9\ M_\odot$, 30% of the total H I mass. Clearly, this model does not correctly reproduce the channel maps at high rotation velocities (top two panels) which appear much thicker in the model than in the data.

4.2. Lagging-halo models

The failure of the two-component model with a co-rotating halo to reproduce the channels near the extreme rotation velocity suggests that the gas above the plane is rotating more slowly than that in the plane, i.e. the halo is lagging in rotation with respect to the disk. Evidence for such a lag was found by Swaters, Sancisi, & van der Hulst (1997) and is also observed in the ionized gas (Heald et al. 2006b; Kamphuis et al. 2007). Fig. 13 shows four models with lagging halos where the rotation velocity decreases with increasing height above the disk. All these models consist of a thin disk (see Fig. 11) and a halo component with the density distribution described above. Table 4 lists the kinematic parameters used in the lagging-halo models. The first model (leftmost column) is that of a lagging halo with the vertical gradient in rotation velocity independent of radius. The rotation curve in the disk is that shown in Fig. 5 (neglecting the inner fast-rotating ring). We have adopted, after a few trials, a constant negative vertical gradient in rotation velocity of $\Delta v_{\rm rot}/\Delta z = -0.55$ km sec^{-1} arcsec^{-1} $\simeq -12$ km sec^{-1} kpc^{-1} for the halo component.

It is clear that this simple lagging-halo model reproduces the main features of the data much better than the previous models. The structure in the upper channel maps is as thin as in the data and it becomes thicker as one approaches the systemic velocity (bottom row).

However, this model is still not completely satisfactory. In particular, near the systemic velocity, the radial extent of the halo gas is much narrower than in the data. One way to improve the model is to increase the velocity dispersion of the halo gas (second column of Fig. 13). For this model all values of the parameters have been kept the same as in the previous model, except the velocity dispersion of the halo gas which has been increased to $\sigma_{\rm halo} = 25$ km sec^{-1} and the halo rotation which has been decreased. The higher velocity dispersion is physically plausible since the gas in the halo is expected to be kinematically "hotter" and to have a more complex motion than the gas in the plane. However, to such increasing velocity dispersion corresponds a decreasing halo rotation and, therefore, an increasing vertical velocity gradient to $\Delta v_{\rm rot}/\Delta z = -0.8$ km sec^{-1} arcsec^{-1} $\simeq -17.4$ km sec^{-1} kpc^{-1}. Fig. 13 shows that increasing the velocity dispersion of the halo gas indeed improves the match of the radial extent of the halo H I in the channel maps close to the systemic velocity (bottom row).

An alternative approach to the increase of the velocity dispersion is to introduce a systematic non-circular motion in addition to the rotation of the halo gas. Such non-circular motions have been found in similar studies of other galaxies. Large-scale inflows toward the galaxy center have been discovered in NGC 2403 ($v_{\rm rad} \sim -15$ km sec^{-1}) (Fraternali et al. 2001) and in NGC 4559 (Barbieri et al. 2005). The third column of Fig. 13 shows the effect of an overall radial motion of the halo of $|v_{\rm rad}| \lesssim 25$ km sec^{-1}. This is of about the same

amplitude as found in NGC 2403 (although in an edge-on galaxy one cannot discriminate between in- and outflow). The models also show that the effects of a higher velocity dispersion or radial motions in the halo are very similar. It is, therefore, not possible to discriminate between an in/outflow and a higher velocity dispersion of the halo gas.

All the models described above do reproduce most of the features present in the data, but do not fully account for the shape of the middle channel maps of NGC 891. Let us focus in particular on the channel map at $v_{\rm hel} = 366.2$ km sec^{-1}. The shape in the data channel map is roughly triangular, while in the models it is more boxy. Clearly, in the model channels near $v_{\rm hel} = 366.2$ km sec^{-1}, there is too much halo emission near the center. In order to obtain the triangular shape, we consider two possibilities. The first is that the inner regions of the halo are depleted of gas (much more than shown in Fig. 10). This obviously would decrease the amount of gas near the center in the models. The second possibility is that the gradient in rotation velocity in the inner parts of the galaxy is larger than in the outer parts. First we consider the possibility of a stronger central gas depletion in the halo. Since the gas density in the halo was derived from the data (without any assumptions about the kinematics), and modeled accordingly, we do not expect the used H I density to be significantly different from the actual one. The main source of errors is the de-projection of the radial profiles. However, this is not expected to have a strong effect beyond $R > 3$ kpc, while in order to reproduce the channel map at $v_{\rm hel} = 366.2$ km sec^{-1} the gas density should be significantly lower than the one used here for radii as large as $R \sim 8$ kpc. Therefore, it seems unlikely that a central depletion is the explanation.

Consider instead the second possibility. The forth column from left in Fig. 13 shows a model (named *shallow rise*) in which the vertical gradient in the rotation velocity varies with R. In the inner regions, the gradient is quite large ($\Delta v_{\rm rot}/\Delta z = -43$ km sec^{-1} kpc^{-1} at $R = 0$), and it decreases linearly with R ($\Delta\left(\Delta v_{\rm rot}/\Delta z\right)/\Delta R \sim 2.5$ km sec^{-1} kpc^{-2}) until it reaches a value of $\Delta v_{\rm rot}/\Delta z = -14$ km sec^{-1} kpc^{-1} and remains constant further out. The shape of the rotation curve of the halo changes with distance from the plane: its inner rising part becomes shallower and shallower. This behavior is illustrated in Fig. 15. Clearly, this model gives a better representation of the channel at $v_{\rm hel} = 366.2$ km sec^{-1} while keeping almost unchanged the other channel maps (note that this shallow-rise model has also a high σ for the halo gas and an inflow similar to the previous two models). The rotation curves for the halo gas at various distances from the plane, derived directly from the observations, will be presented and discussed by Fraternali (2007, in preparation).

We further compare the models by inspecting the position-velocity cuts perpendicular to the major axis of the galaxy. Fig. 14 shows two sets of such cuts taken on the NE side of the galaxy at a distance of $1'$ (2.8 kpc, bottom) and $2.7'$ (7.5 kpc, top) from the center.

The emission shows a characteristic triangular shape. The thin-disk is visible at all velocities between systemic ($v_{\rm hel} = 528$ km sec^{-1}) and the maximum rotation ($v_{\rm hel} \sim 290$ km sec^{-1}), whereas the halo appears to have its maximal extent near the systemic velocity. It is clear that the shallow-rise model best reproduces the triangular shape as well as the difference between the $1'$ and $2.7'$ plots. The white squares in the data plots show the rotational velocities adopted for the shallow-rise model.

The comparison of the various models leads to the conclusions that the thin disk of NGC 891 is surrounded by an extended gaseous halo which is rotating more slowly than the disk and contains almost 30% of the neutral gas of the galaxy. The kinematics of the gas in the halo can be best explained by assuming a vertical gradient in the rotation velocity. Moreover, this gradient is stronger in the inner regions ($\Delta v_{\rm rot}/\Delta z \simeq -43$ km sec^{-1} kpc^{-1}) than at larger radii ($\Delta v_{\rm rot}/\Delta z \simeq -14$ km sec^{-1} kpc^{-1}. Finally, the velocity dispersion of the halo gas is higher than that of the gas in the disk ($\sigma_{\rm halo} \simeq 20 - 25$ km sec^{-1} vs $\sigma_{\rm disk} \simeq 8$ km sec^{-1}) and/or there are significant radial motions in the halo gas ($|v_{\rm rad}| \lesssim 25$ km sec^{-1}).

5. Discussion

In the previous Section we have studied with 3-D models the extended extra-planar H I emission of NGC 891 and concluded that this galaxy has a massive halo of neutral gas rotating more slowly than the disk. Here we discuss the properties of this H I halo, its possible origins and the comparison with data at different wavelengths.

5.1. The structure of the H I halo

The H I halo of NGC 891 is the most extended and massive of those found to date in a spiral galaxy (Fraternali et al. 2007a). The H I mass above $z = 1$ kpc is about 30% of the total H I mass. The distribution of gas in the halo appears fairly symmetric and regular in the four quadrants of the galaxy up to about 8 kpc from the plane (Figs. 1 and 2). **In three quadrants, the H I extends further up to about 14 kpc, whereas the N-W quadrant is dominated by an extended filament reaching up to $8'$ ($\sim$22 kpc). Radially, the halo extends to the end of the disk on the N-E side but stops earlier on the S-W side where the disk is more extended.** This may be an indication that the halo is closely connected to the inner disk of NGC 891.

Also the kinematics of the halo is symmetric and regular in the four quadrants **up to a height of about 8 kpc** (Fig. 3). The gradient in rotation velocity can be measured up

to about 5 kpc. Above that the rotation velocity continues to decrease further, but the gas density is too low to derive reliable rotation velocities (Fraternali et al. 2005). The gas in the halo may have radial motions and/or higher velocity dispersion than the disk gas, as the above model analysis indicates (Section 4.2). Vertical motions may also be present (as in NGC 2403, Fraternali et al. (2001)) but because of the inclination of the galaxy they cannot be observed.

The halo of NGC 891 shows individual features (streams and compact clouds) somewhat "separated" either in location or kinematics from its main bulk. The most prominent feature is the extended filament in the N-W quadrant (see Figs. 1 and 4). This feature has a mass of more than 1.6×10^7 $M_\odot$, it extends out to a projected radius of about 10 kpc from the center of the galaxy and vertically up to 22 kpc (Figs. 4, 16). The full length of the filament is about 30 kpc, its velocity width is $\Delta_{\rm v} \lesssim$ 100 km sec^{-1} and its mean velocity is close to systemic for $z \gtrsim 10$ kpc.

A key question is whether the H I halo of NGC 891 is a diffuse medium (filling factor ~ 1) or it is entirely made of discrete *compact* clouds. A first inspection of the datacube seems to indicate that most of the gas belongs to a smooth and coherent, differentially rotating structure. This picture of a "diffuse medium" may, however, be erroneous and be produced, at least to some extent, by projection effects along the line of sight. Only clouds with anomalous velocities or located at large distances from the plane would stand out clearly (**such as those shown in** Fig. 16). These clouds, together with the filament on the NW quadrant may be evidence that the halo of NGC 891 is indeed made, at least partly, of individual gas complexes. These complexes would be similar to those observed in non–edge-on galaxies like NGC 2403 and NGC 6946 where projection effects are less important (Fraternali et al. 2002; Boomsma et al. 2005a; Boomsma 2007). Moreover, they would have similar properties as the HVCs and IVCs of the Milky Way (Wakker & van Woerden 1997) and the clouds seen near M31 (Westmeier, Braun, & Thilker 2005). A structure like the long NW filament would probably appear as a "Complex A" or "Complex C" of the HVCs to an observer inside NGC 891.

5.2. Origin of the H I halo

What is the origin of the H I halo of NGC 891? We discuss here two possibilities: the galactic fountain and the accretion from outside. The main observational facts to be accounted for are: 1) the halo is very extended and massive (about 30% of the total H I mass); 2) the halo kinematics is dominated by differential rotation and the rotation velocity decreases with height from the plane; 3) a high velocity dispersion or non-circular motions

(maybe inflow?) are also present; 4) the halo is structured in clouds and filaments, some of which are at very anomalous (counter-rotating) velocities; **5) As the distance from the plane increases, the radial distribution of the gas in the halo tends to become flatter and less concentrated to the center than in the disk. On the southern side, the halo is radially less extended than the disk.**

5.2.1. Fountain

There is considerable evidence from Hα radio continuum and X-ray data pointing at a galactic fountain mechanism playing a major role in forming the gaseous halo of NGC 891. The Hα image of NGC 891 (Dettmar 1990; Rand 1990) indicates that the star formation rate in the disk, especially on its northern side, is very high. There is strong radio continuum emission (thermal and non-thermal) in the disk and also (non-thermal) in the halo, extending up to ∼10 kpc from the plane (see Fig. 8). This extent is close to that of the H I halo and indicates the presence of magnetic fields and relativistic electrons in correspondence of the H I gas. Also, there is a clear correlation between this radio emission and the Hα halo (Dettmar 1990; Rand 1990; Dahlem, Dettmar & Hummel 1994). In particular, the northern side of the galaxy is much brighter in both components and in the NW quadrant the radio halo has a larger scaleheight (Fig. 9). A corresponding N-S asymmetry is also seen in the H I halo. Fig. 6, which shows the thickness of the H I layer as a function of position and velocity, indicates that in the inner regions of the disk (corresponding to small R and velocities furthest away from systemic), the H I disk is thicker on the northern (i.e. approaching) than on the southern side. The northern side of the disk is where star formation and consequently the fountain are strongest.

The ionized gas in the halo of NGC 891 has a smooth component (Diffuse Ionized Gas) but it also shows filamentary structures (Howk & Savage 2000). **Collimated** Hα **filaments are seen reaching up to more than 2 kpc from the plane (Rossa et al. 2004). Moreover, the radio emission is strongly polarized. Both these features suggest the presence of a uniform magnetic field in the halo, indicating that the outflowing gas has also torn the** B**-field out of the disk (Dahlem, Dettmar & Hummel 1994)**. Interestingly, also the long H I filament found in our data is similarly oriented. However, in the Hα images there is no trace of an ionized counterpart of the H I filament **to the detection limit**.

Hot coronal gas was first revealed in NGC 891 by ROSAT (Bregman & Pildis 1994). Recently, Chandra **and XMM** data have confirmed this detection and have shown the presence of filamentary substructures in the halo component extending up to about 5-6 kpc

from the plane (Strickland et al. 2004) **while the soft halo component seems to be concentrated to the inner disk (Tüllmann et al. 2006a)**. These authors were able to show for a sample of galaxies, including NGC 891, that the amount of hot gas is proportional to the mechanical feedback from supernovae, concluding that this hot gas is almost certainly produced by a fountain. The X-ray emission also correlates fairly well with the Hα emission (Rossa et al. 2004), and the X-ray spectrum of the halo emission in the range 0.3−2 keV is fitted by a plasma with a temperature of 0.23 keV (3.7×10^6 K).

Besides the H I there are in NGC 891 also other "cold" extra-planar components such as dust and CO. The dust shows up as absorption features against the star light up to heights of about 2 kpc (Howk & Savage 1997, 2000). Such features have masses of about 10^5 $M_\odot$ (using the galactic dust-to-gas ratio). **This cold medium does not seem to correlate, on small spatial scales,** with the warm medium observed in Hα (Howk & Savage 2000; Rossa et al. 2004); thus the two phases appear to be **physically** distinct. CO emission is also observed up to about 2 kpc from the plane of NGC 891 (Garcia-Burillo et al 1992; Sofue & Nakai 1993). This extra-planar component of molecular gas comprises about a 35% of the total amount of molecular gas.

All this evidence suggests that a classical galactic fountain (ionized outflow, cooling, and cold inflow) is active in NGC 891 and is responsible for much of the gaseous components, at least in the lower halo ($z \lesssim 5$ kpc). These components have a total mass of the order of a few $\times$ 10^8 $M_\odot$. Among them, the H I halo is the most massive and the most extended reaching a distance from the plane of more than 20 kpc. This latter may be the result of an observational bias or the indication that a different mechanism, perhaps accretion from outside (see below), is responsible for the formation of the upper layers.

Galactic fountain models can easily explain the distribution of the H I in the halo of NGC 891, with the exception of the extended filament (see below). Indeed, only a few percent of the energy from supernovae would be sufficient (Fraternali & Binney 2006). However, such models fail to reproduce the kinematics of the halo gas (both ionized and H I). The ionized component has been initially studied using long-slit spectroscopy (Rand 1997) and more recently using the WIYN integral field unit (Heald et al. 2006b) **and TAURUS spectroscopy (Kamphuis et al. 2007)**. The gradient in rotation velocity derived for the ionized gas in the latter study is in good agreement with that observed in H I about -15 km sec^{-1}kpc^{-1} for $1 < z < 5$ kpc. This result indicates that the H I and Hα phases are part, at least in the lower halo, of the same phenomenon and, therefore, probably also have the same origin. A similar coupling between ionized and neutral halo gas has also been found in the spiral galaxy NGC 2403 (Fraternali, Oosterloo & Sancisi 2004). This observed gradient in rotation velocity with z is significantly higher than predicted by the fountain models

(Fraternali & Binney 2006; Heald et al. 2006b). The only way to reconcile these models with the data is to find a mechanism that would make the fountain gas loose part of its angular momentum. One possibility is that it is braked by the hot halo. However, in this case, the angular momentum transfer to the hot halo would speed it up very quickly (Fraternali et al. 2007b). A second, more promising possibility is that the fountain gas interacts with low angular momentum material accreted from the IGM (Fraternali & Binney, in preparation).

5.2.2. External origin

It is clear from the foregoing discussion that a "fountain" origin for most of the H I in the halo of NGC 891 is very likely. But a continuous supply of low angular momentum material from outside may also be needed to account for the observed H I kinematics. The amount of accreted gas, however, can be small, perhaps not more than 10 percent of the gas present in the halo (Fraternali & Binney, in preparation).

Is there any direct observational evidence of such gas infall in NGC 891? An obvious candidate for accretion is the filament in the NW quadrant extending up to 22 kpc from the plane. As mentioned above, this filament has a projected velocity close to systemic. This may indicate either of these two possibilities: 1) the filament belongs to the inner parts of the halo and has a very small z component of the angular momentum or 2) it is located in the far outer parts of the halo. For the filament to be produced by a galactic fountain, one would require very high kick velocities and a very high initial kinetic energy. Using the galactic fountain model of Fraternali & Binney (2006), we estimate that the required kick velocities to send material up to $z = 15$ kpc range from 240 km sec^{-1} for a starting radius of 10 kpc to 425 km sec^{-1} for a starting radius of $R = 2$ kpc. For a mass of the filament of $1.6{\times}10^7$ $M_\odot$, the kinetic energies would be $1 - 3 \times 10^{55}$ erg. Therefore, to produce such a filament in one single event, hundreds of thousands of supernovae would be required. This seems quite unlikely. If instead the gas complex had an external origin, its filamentary structure and its kinematics might be more easy to explain: a cloud falling onto NGC 891 would be stretched out and might speed up to full rotation as it gets close to the disk.

An external origin for the filament may be as cold accretion from the IGM. Or it may be through a condensation of the hot coronal gas, possibly triggered by the galactic fountain. Alternatively, the filament could be the result of the merging of a companion with NGC 891. The stellar part of the companion could be elsewhere or too faint to be seen and the filament would be the only prominent remnant of the process. In this respect we note that deep H I observations are a powerful tool to look for this kind of events and could be used to detect merging at much larger distances than optical data.

Finally, we note that the filament roughly points at the projected position of the companion UGC 1807 (Fig. 7) and one may wonder whether it could have originated from a close encounter of UGC 1807 with NGC 891. The filament would have to be either gas pulled up from the outer disk of NGC 891 or gas stripped from the companion. This is not impossible, in spite of the present large separation of UGC 1807 from NGC 891 and of its symmetrical structure and kinematics, which would seem to exclude recent tidal encounters. The projected distance of about 80 kpc could have been covered by the companion with a velocity of 100−200 km sec^{-1} in 8−4 $\times$ 10^8 yrs. This is sufficiently longer than the dynamical time scales in the outer parts of the companion (2 $\times$ 10^8 from 100 km sec^{-1} rotation at 4 kpc radius) to account for the absence of any sign of disturbances. On the other hand, the filament, presumably located in the outer parts of NGC 891, would have survived long enough to be observed now. In this connection it is interesting to draw attention to another puzzling, long-known structure revealed by the H I observations of NGC 891: the extended southern tail. This is difficult to maintain for a long time against the effect of differential rotation (Baldwin, Lynden-Bell & Sancisi 1980) and the possibility of a recent origin (less than 1 $\times$ 10^9 yrs) would therefore be quite attractive. It is therefore interesting to ask whether a tidal encounter with UGC 1807, as considered here for the origin of the filament, could also be responsible for the north-south H I lopsidedness of NGC 891. Note that the mass of the companion ($\sim$10% of that of NGC 891) is not negligibly small.

Other indications of accretion are the counter-rotating clouds shown in Fig. 16. These clouds cannot be produced by a galactic fountain as they have an orientation of the angular momentum opposite to the gas in the disk. They are almost certainly located in the outer halo (one is observed at a projected distance of 28 kpc), otherwise the drag by the co-rotating H I would have quickly inverted their motion. Note that one of these cloud complexes is spatially (and kinematically) very close to the filament. The total H I mass present in those accreting clouds (filament included) is of a few 10^7 $M_\odot$. Considering a typical infalling time of the order of 10^8 yr, this would correspond to an accretion rate of $\approx$ 0.1 $M_\odot$yr^{-1}. This latter should be considered as a lower limit to the total accretion rate as most of the accreting material may be impossible to detect after it has interacted with the fountain halo.

6. Summary of results

The deep H I observations of NGC 891 reported here have shown the following:

1. The H I halo is considerably more extended than shown in previous observations. It is detected out to a vertical distance of about 22 kpc from the galactic plane and contains 1.2 $\times$ 10^9 $M_\odot$ amounting to about 30% of the total H I. The halo is not smooth. It shows

structures on various scales and there are, in particular, also H I clouds with very anomalous (counter-rotating) velocities. These have masses of about 1×10^6 $M_\odot$. Furthermore, there is a striking long filament extending (in projection) up to more than 20 kpc from the disk and containing more than 1.6 $\times 10^7$ $M_\odot$.

2. The H I halo has overall regular differential rotation but it rotates more slowly than the disk (as already found by Swaters, Sancisi, & van der Hulst (1997)). The vertical gradient of the rotational velocity is about -15 km sec^{-1} kpc^{-1}. The shape of the halo rotation curves does not remain constant with distance from the plane, but its rising part becomes shallower and shallower with height. Random motions in the halo or systematic deviations from circular motion (in- or out-flows) may also be present.

3. A significant fraction of the H I halo must come from a galactic fountain, as the high star formation rate in the disk strongly suggests. The radio continuum, the Hα and the X-ray data are all corroborating evidence. However, the kinematics of the halo suggests the need of an interaction between the fountain gas and low angular momentum material. Such material may be supplied by gas accretion from the surrounding IGM. The long H I filament and the counter-rotating clouds may be direct evidence of such accretion.

The WSRT is operated by the Netherlands Foundation for Research in Astronomy (ASTRON) with the support from the Netherlands Foundation for Scientific Research (NWO). This research has made use of the NASA Extragalactic Database (NED), whose contributions to this paper are gratefully acknowledged. The Digitized Sky Survey was produced at the Space Telescope Science Institute under US Government grant NAG W-2166. We thank Richard Rand and George Heald for providing the information about their Hα data and George Heald for providing his version of GALMOD.

REFERENCES

Allen, R.J., Sancisi, R., Baldwin, J.E., 1978, A&A, 62, 397

Baldwin, J.E., Lynden-Bell, D., Sancisi, R. 1980, MNRAS, 193, 313

Barbieri, C.V., Fraternali, F., Oosterloo, T., Bertin, G., Boomsma, R., Sancisi, R. 2005, A&A, 439, 947

Barnabè M., Ciotti, L., Fraternali, F., Sancisi, R., 2006, A&A, 446, 61

Becquaert, J.-F., Combes, F. 1997, A&A, 325, 41

Benjamin, R.A., 2002, in Seeing Through the Dust ed. A.R. Taylor, T.L. Landecker, and A.G. Willis, ASP Conference Series, Vol. 276, 201

Boomsma, R., Oosterloo, T., Fraternali, F., van der Hulst, J.M., Sancisi, R., 2005, ASPC, 331, 247; proceeding of "Extra-planar Gas", Dwingeloo, 2004 (astro-ph/0410022)

Boomsma, R.; Oosterloo, T. A.; Fraternali, F.; van der Hulst, J. M.; Sancisi, R. 2005, A&A, 431, 65

Boomsma, R. 2007, PhD Thesis, University of Groningen

Braun, R., Thilker, D., Walterbos, R.A.M. 2003, A&A, 406, 829

Bregman, J.N., 1980, ApJ, 236, 577

Bregman, J.N.; Pildis, R.A., 1994, ApJ, 420, 570

Collins, J.A., Benjamin, R.A., Rand, R.J., 2002, ApJ, 578, 98

Dahlem, M., Dettmar, R.-J., Hummel, E. 1994, A&A, 290, 384

Dahlem, M., Lisenfeld, U., Rossa, J. 2006, A&A, 457, 121

Dettmar, R.-J. 1990, A&A, 232, 15

de Vaucouleurs G., de Vaucouleurs A., Corwin H. G., Buta R. J., Paturel G., Fouque P. 1991, Third Reference Catalog of Bright Galaxies, Vols. 13, XII. Springer-Verlag, (RC3)

Fraternali, F., Oosterloo, T., Sancisi, R., Van Moorsel, G. 2001, ApJ, 562, L47

Fraternali, F., Van Moorsel, G., Sancisi, R., Oosterloo T. 2002, AJ, 123, 3124

Fraternali, F., Oosterloo, T., Sancisi, R. 2004, A&A, 424, 485

Fraternali, F., Oosterloo, T., Sancisi, R., Swaters, R.A. 2005, ASPC, 331, 239; proceeding of "Extra-planar Gas", Dwingeloo, 2004

Fraternali, F., Binney, J.J., 2006, MNRAS, 366, 449

Fraternali F., Oosterloo T., Binney, J.J., Sancisi R. 2007, Island Universes, p. 271, ed. R.S. de Jong, Springer (astro-ph/0510734)

Fraternali, F., Binney, J.J., Oosterloo T., Sancisi R. 2007, New Astronomy Review, Vol. 51; proceedings of "The Fate of Gas in Galaxies", Dwingeloo, July 2006

Garcia-Burillo, S., Guelin, M., Cernicharo, J., Dahlem, M. 1992, A&A, 266, 21

Garcia-Burillo, S., Guelin, M. 1995, A&A, 299, 657

Gentile, G., Fraternali, F., Klein, U., Salucci, P., 2003, A&A, 405, 969

Heald, G.H., Rand, R.J., Benjamin, R.A., Collins, J.A., Bland-Hawthorn, J., 2005, ApJ 2006, ApJ, 636, 181

Heald, G.H., Rand, R.J., Benjamin, R.A., Bershady M.A. 2006, ApJ, 647, 1018

Heald, G.H., Rand, R.J., Benjamin, R.A., Bershady M.A. 2006, ApJ, in press (astro-ph/0703324)

Hoopes, C.G., Walterbos, R.A.M., Rand, R.J. 1999, ApJ, 522, 669

Howk, J.C., Savage, B.D. 1997, AJ, 114, 2463

Howk, J.C., Savage, B.D. 2000, AJ, 119, 644

van der Hulst J.M., Sancisi R. 1988, AJ, 95, 1354

van der Hulst J.M., Sancisi R. 2005, ASPC, 331, 139

Kamphuis, P., Peletier, R.F., Dettmar, R.-J., van der Hulst, J.M., van der Kruit, P.C., Allen, R.J. 2007, A&A, in press (astro-ph/0703363)

Kaufmann, T., Mayer, L., Wadsley, J., Stadel, J., Moore, B. 2006, MNRAS, 370, 1612

van der Kruit, P.C. 1981, A&A, 99, 298

van der Kruit, P.C. 1984, A&A, 140, 470

Lee, S.-W., Irwin, J.A., Dettmar, R.-J., Cunningham, C.T., Golla, G., Wang, Q.D., 2001, A&A, 377, 759

Maloney, P. 1993, ApJ, 414, 41

Matthews, L.D., Wood, K., 2003, ApJ, 593, 721

Naab, T., Ostriker, J.P. 2006, MNRAS, 366, 899

Popescu, C.C., Tuffs, R.J., Kylafis, N.D., Madore, B.F., 2004, A&A, 414, 45

Rand, R.J., Kulkarni, S.R., Hester, J.J. 1990, ApJ, 352, 1

Rand, R.J. 1997, ApJ, 474, 129

Rand, R.J. 2000, ApJ, 537, L13

Rossa, J.; Dettmar, R.-J. 2003, A&A, 406, 505

Rossa, J.; Dettmar, R.-J., Walterbos, R.A.M.; Norman, C.A. 2004, AJ, 128, 674

Rupen, M.P. 1991, AJ, 102, 48

Sancisi, R., Allen, R.J. 1979, A&A, 74, 73

Sault, R.J., Teuben, P.J., Wright, M.C.H. 1995, in Astronomical Data Analysis Software and Systems IV, R. Shaw, H.E. Payne and J.J.E. Hayes, eds, Astronomical Society of the Pacific Conference Series, 77, p. 433

Schaap, W.E., Sancisi, R., Swaters, R.A., 2000, A&A, 356, L49

Shapiro, P.R., Field, G.B., 1976, ApJ, 205, 762

Shaw, M.A., Gilmore, G., 1989, MNRAS, 237, 903

Sofue, Y., Nakai, N. 1993, PASJ, 45, 139

Sommer-Larsen, J. 2006, ApJ, 644L, 1

Strickland, D.K., Heckman, T.M., Colbert, E.J.M., Hoopes, C.G., Weaver, K.A. 2004, ApJS, 151, 193

Swaters, R.A., Sancisi, R., & van der Hulst J. M. 1997, ApJ, 491, 140

Thilker, D.A.; Braun, R.; Walterbos, R.A.M.; Corbelli, E.; Lockman, F.J.; Murphy, E.; Maddalena, R. 2004 ApJ, 601, 39

Tripp, T.M., Wakker, B.P., Jenkins, E.B., Bowers, C.W., Danks, A.C., Green, R.F., Heap, S.R., Joseph, C.L., Kaiser, M.E., Linsky, J.L., Woodgate, B.E., 2003, AJ, 125, 3122

Tüllmann, R., Dettmar, R.-J., Soida, M., Urbanik, M., Rossa, J. 2000, A&A, 364, L36

Tüllmann, R., Pietsch, W., Rossa, J., Breitschwerdt, D., , W., Dettmar, R.-J. 2006, A&A, 448, 43

Tüllmann, R., Breitschwerdt, D., Rossa, J, Pietsch, W., Dettmar, R.-J. 2006, A&A, 457, 779

van der Hulst, J.M., Terlouw, J.P., Begeman, K.G., Zwitser, W., Roelfsema, P.R. 1992, ASP Conf. Ser. 25: Astronomical Data Analysis Software and Systems I, 25, 131

Wakker B.P, van Woerden H., 1997, ARA&A, 35, 217

Wakker, B.P. 2001, ApJS, 136, 463

Westmeier, T., Braun, R., Thilker, D. 2005, A&A, 436, 101

White, S.D.M., Frenk, C.S. 1991, ApJ, 379, 52

Table 1. Optical and radio parameters for NGC 891.

	NGC 891	ref
Morphological type	Sb/SBb	1,2
Radio continuum centre (α, δ J2000)	$2^{\rm h}\ 22^{\rm m}\ 33.0^{\rm s}$	5
	$42^\circ\ 20'\ 57.2''$	5
Distance (Mpc)	9.5	1
L_B ($L_{\odot\,B}$)	$2.6{\times}10^{10}$	3
Scale length stellar disk(kpc)	4.4	4
SFR ($M_\odot\,{\rm yr}^{-1}$)	3.8	6
Systemic velocity (km s^{-1})	528 ± 2	5
Total H I mass ($M_\odot$)	4.1×10^9	5
H I inclination ($^\circ$)	$\gtrsim 89$	5
Mean P.A. (no warp) ($^\circ$)	23°	5
Total mass ($M_\odot$)	1.4×10^{11}	5

References. — (1) van der Kruit (1981), (2) Garcia-Burillo & Guelin (1995), (3) de Vaucouleurs et al. (1991), (4) Shaw & Gilmore (1989), (5) This work, (6) Popescu et al. (2004)

Table 2. Observational parameters for NGC 891.

	NGC 891
Observation dates	Aug. - Dec. 2002
Total length of observation (hr)	20 × 12
Effective integration time (hr)	204
Pointing R.A. (J2000)	$2^{h}\ 22^{m}\ 33.76^{s}$
Pointing Dec (J2000)	$42^{\circ}\ 20'\ 57.1''$
Velocity centre of band (km sec^{-1})	800
Total bandwidth (MHz)	10
Total bandwidth (km sec^{-1})	∼2000
Number of channels in observation	1024
Channel separation in observation (kHz)	9.77
Number of channels of final datacube	224
Channel separation of final datacube (kHz)	38.5
Velocity resolution (after Hanning) (km sec^{-1})	16.4

Table 3. Parameters of the data cubes.

	Full resolution	Intermediate resolution	Low Resolution
Spatial resolution ($''$)	23.4×16.0	33.2×23.9	69.6×58.9
P.A. of synthesized beam ($^\circ$)	12.3	16.0	16.0
Beam size (kpc)	1.08×0.74	1.53×1.09	3.2×2.7
R.m.s. noise per channel (mJy beam^{-1})	0.090	0.10	0.12
Minimum detectable column density (3σ; cm^{-2})	13.0×10^{18}	6.8×10^{18}	1.6×10^{18}
Minimum detectable mass (3σ; $M_\odot$ per resolution element)	9.3×10^4	1.0×10^5	1.3×10^5

Table 4. Parameters of the lagging-halo models shown in Figs. 13 and 14.

Model	$\Delta V_{\rm rot}/\Delta z$ (km sec^{-1} kpc^{-1})	$\sigma_{\rm gas}$ (km sec^{-1})	$v_{\rm rad}$ (km sec^{-1})
Lagging halo	-12.0	8	0
High σ	-17.4	25	0
Inflow	-13.0	8	-25
Shallow rise	$-43.0 \rightarrow -14.0$	20	-15

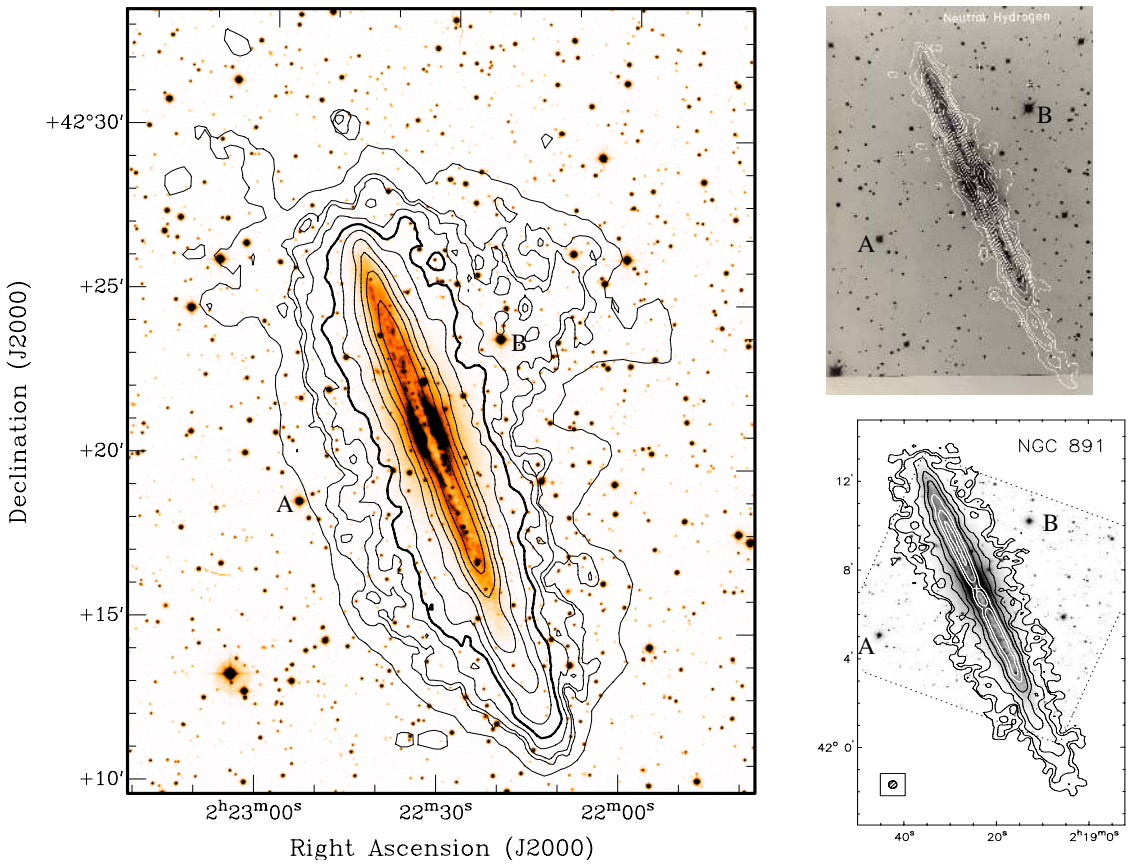

Fig. 1.— **Left: total H I image as obtained from the observations described in this paper. The outer grey contour comes from the** $60''$ **data and its level is** $0.005 \cdot 10^{21}$ **cm**$^{-2}$**. The black contours come from the** $30''$ **data with contour levels 0.01, 0.02, 0.05, 0.1 (thick line), 0.2, 0.5, 1.0, 2.0 and** $5.0 \cdot 10^{21}$ **cm**$^{-2}$**. For comparison of the total H I images of NGC 891 published over the years, we show the one from Sancisi & Allen (1979) (top right) with spatial resolution of about** $30''$ **and contour levels of 0.5, 1.0, 1.5, 2.4, 4.1, 5.7, 7.3, 8.9 and** $10.5 \cdot 10^{21}$ **cm**$^{-2}$ **and the total H I image as published by Swaters, Sancisi, & van der Hulst (1997) (bottom right). The spatial resolution of the last image is about** $20''$ **and the contour levels are 0.07, 0.17, 0.46, 1.1, 2.3, 4.1, 6.4 and** $9.2 \cdot 10^{21}$ **cm**$^{-2}$**. To aid the comparison, two stars labeled 'A' and 'B' are marked in each figure**

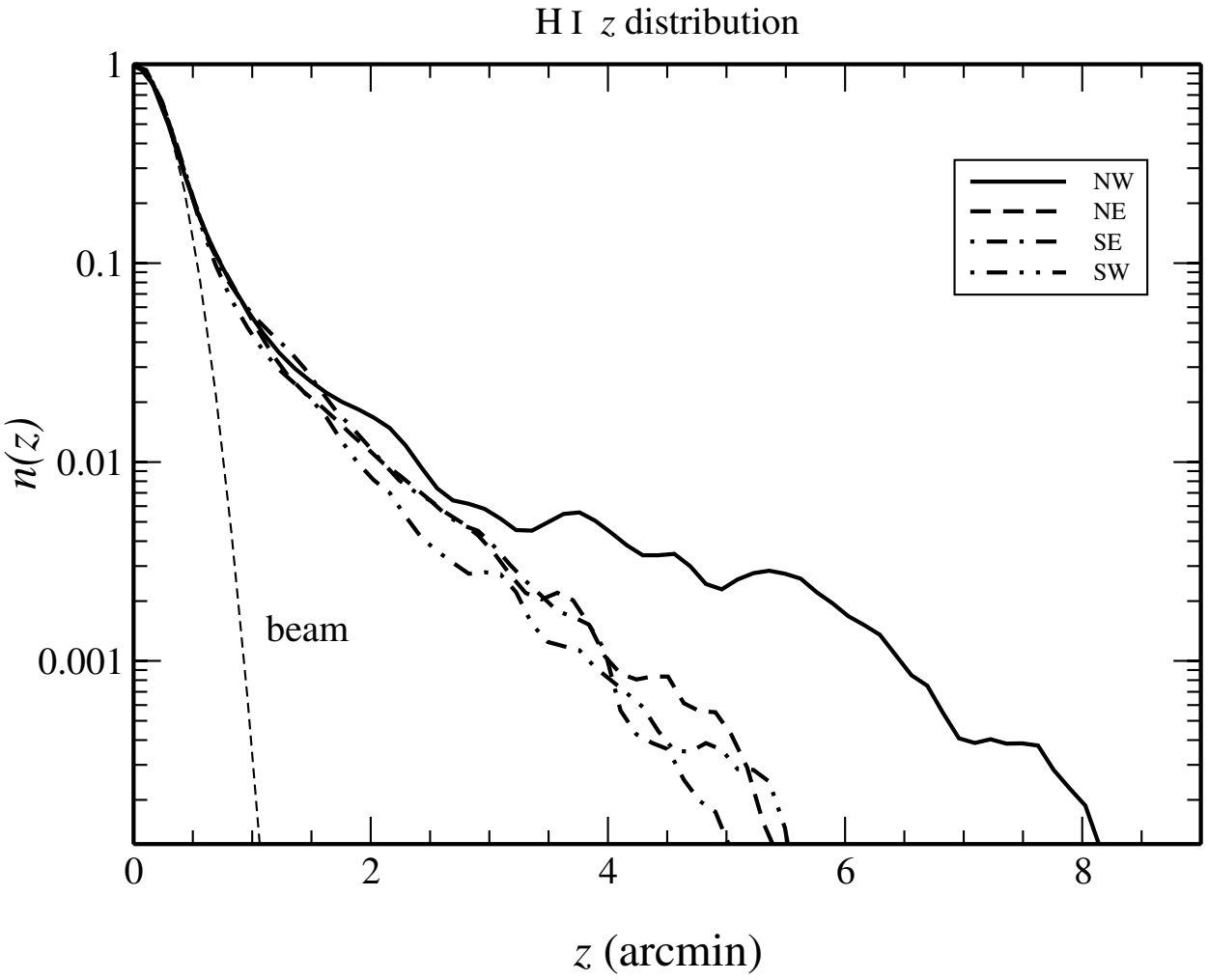

Fig. 2.— Normalized average H I column densities along the z direction for the four quadrants of NGC 891. The spatial resolution of the observations is indicated. ($1'$ corresponds to 2.76 kpc)

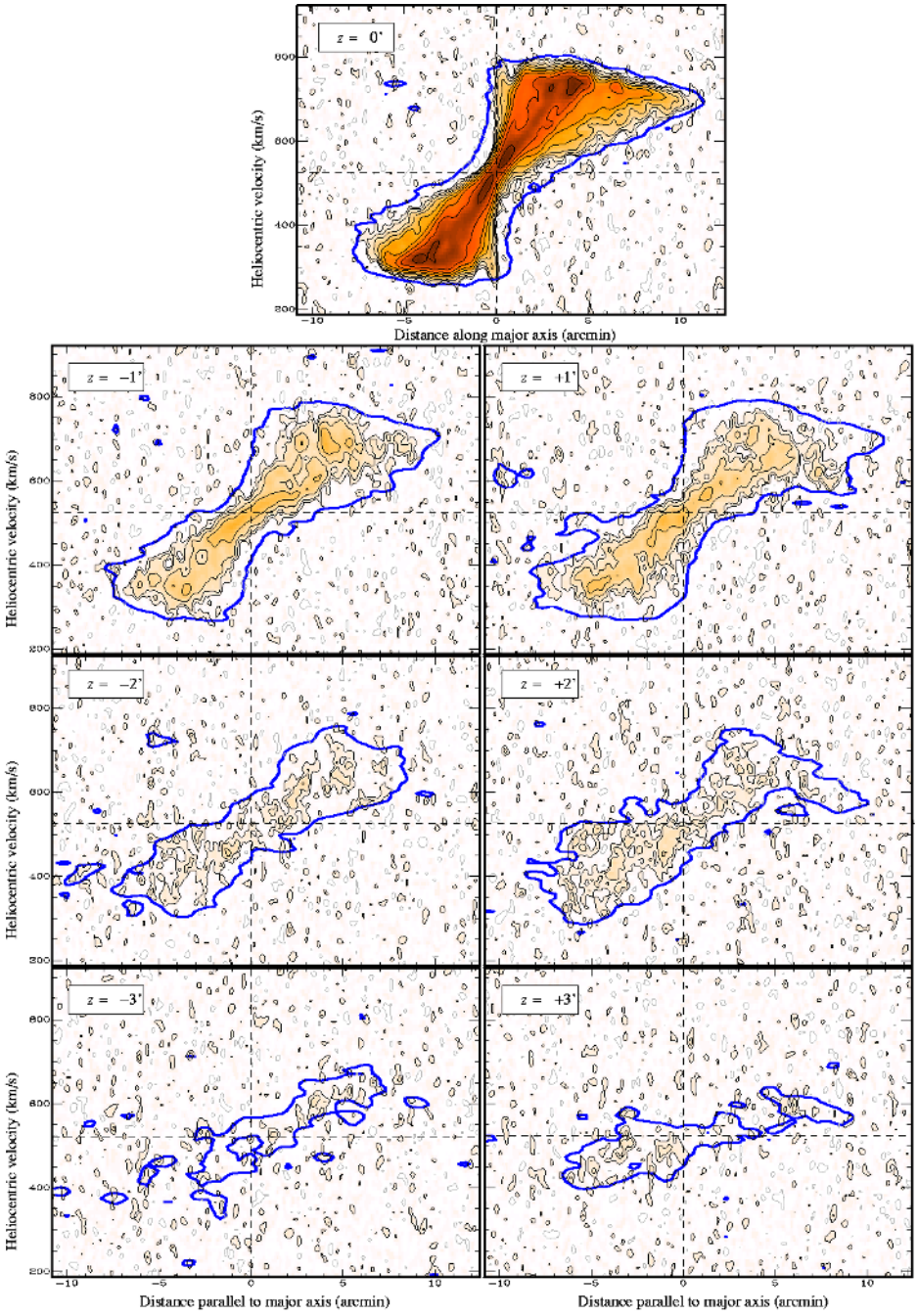

Fig. 3.— Position-velocity plots parallel to the plane for NGC 891 made from the high-resolution data cube (thin lines and greyscale) and the 60-arcsec data (thick line) Contour levels are in steps of 1.5σ for the high-resolution data and at 3σ for the low-resolution data.

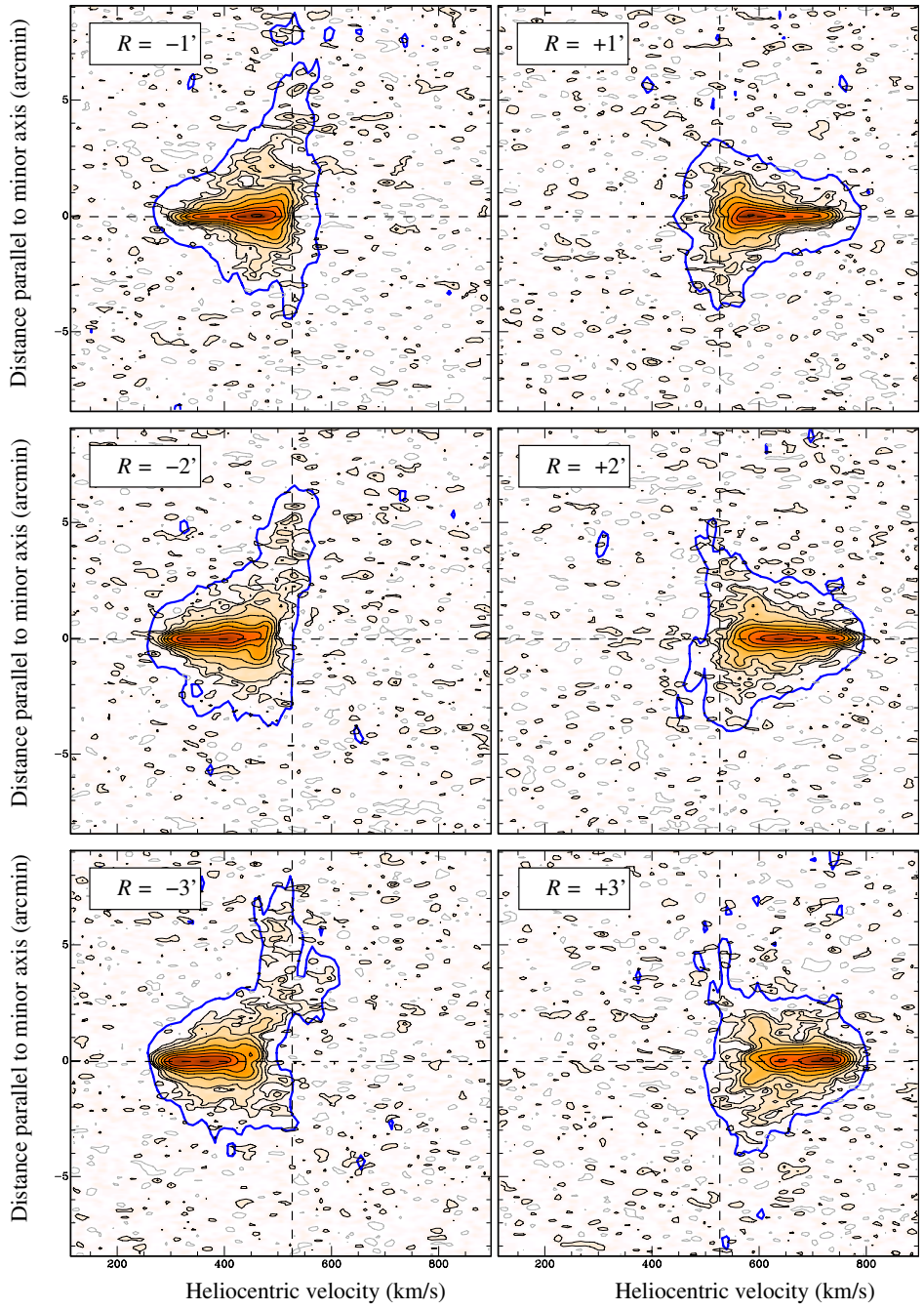

Fig. 4.— Position-velocity plots perpendicular to the plane for NGC 891 made from the high-resolution data cube (thin lines and greyscale) and the 60-arcsec data (thick line). Contour levels are in steps of 1.5σ for the high-resolution data and at 3σ for the low-resolution data.

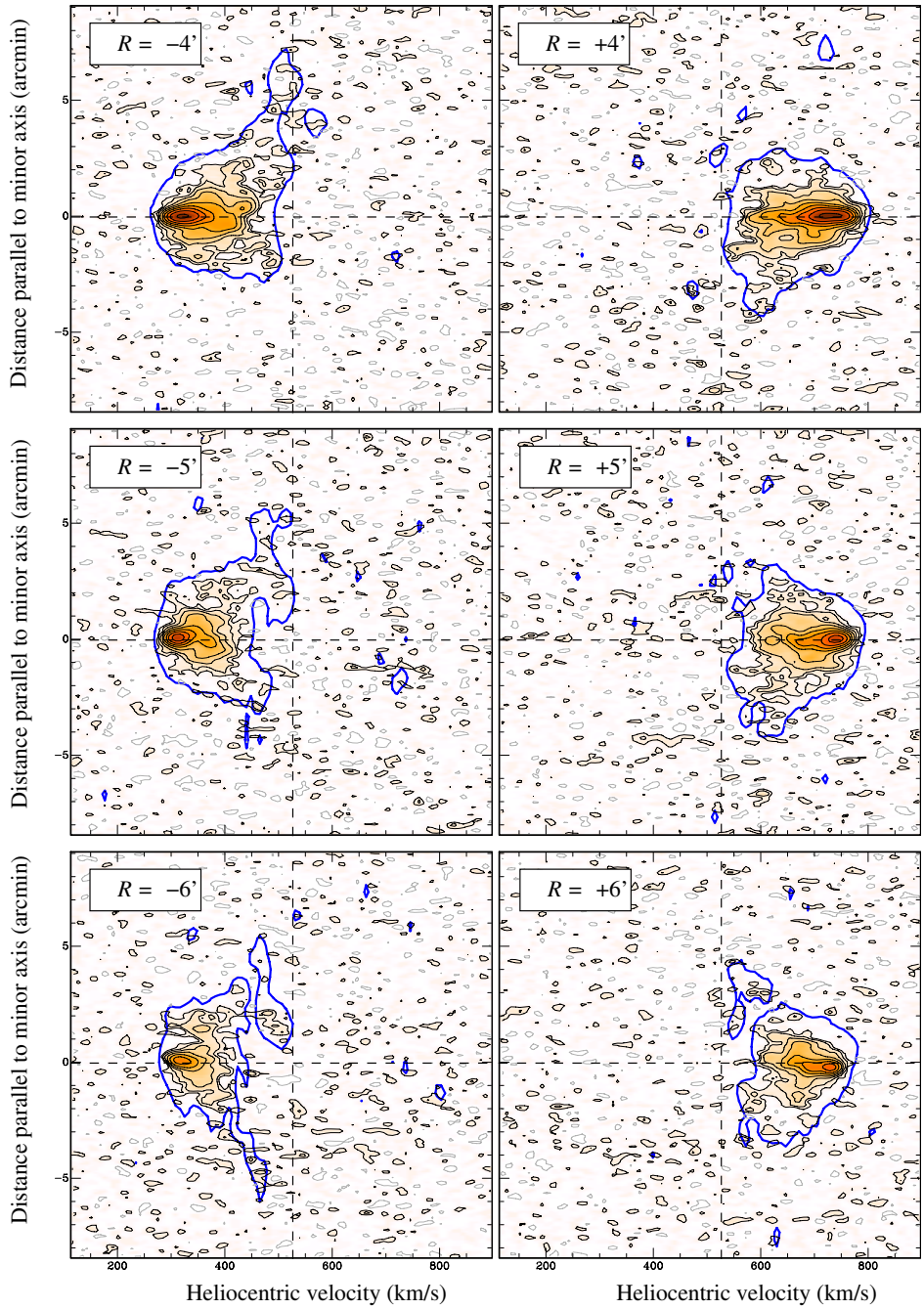

Fig. 4 (cont'd).— Position-velocity plots perpendicular to the plane for NGC 891 made from the high-resolution data cube (thin lines and greyscale) and the 60-arcsec data (thick line). Contour levels are in steps of 1.5σ for the high-resolution data and at 3σ for the low-resolution data.

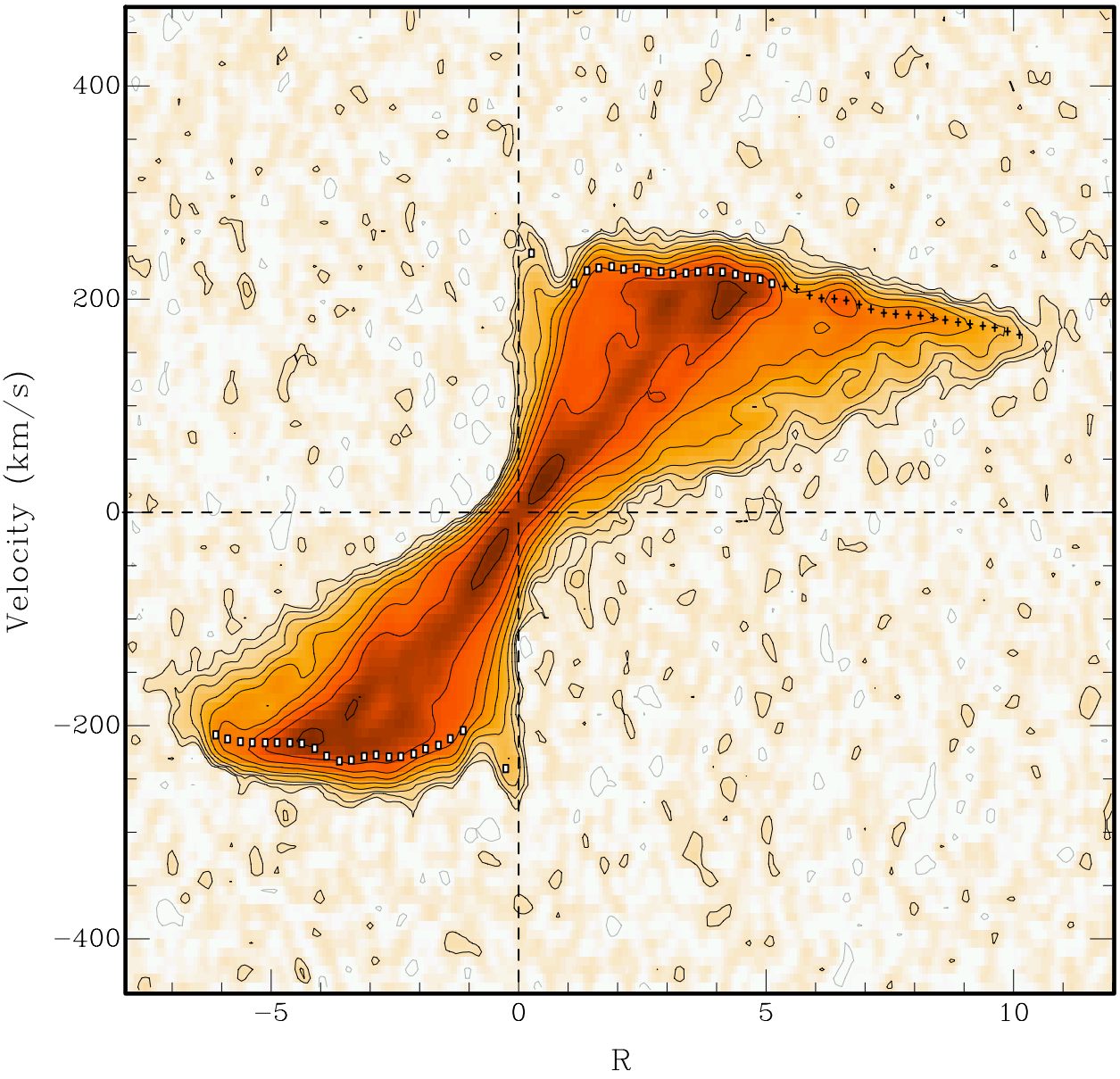

Fig. 5.— Position-velocity diagram taken along the major axis of the full-resolution data. The open squares show the rotation curve determined for the N and S side independently, while the crosses indicate the velocities for the SW extention of the galaxy. Contour levels are –0.135, 0.135, 0.27, 0.54, ... mJy beam^{-1}.

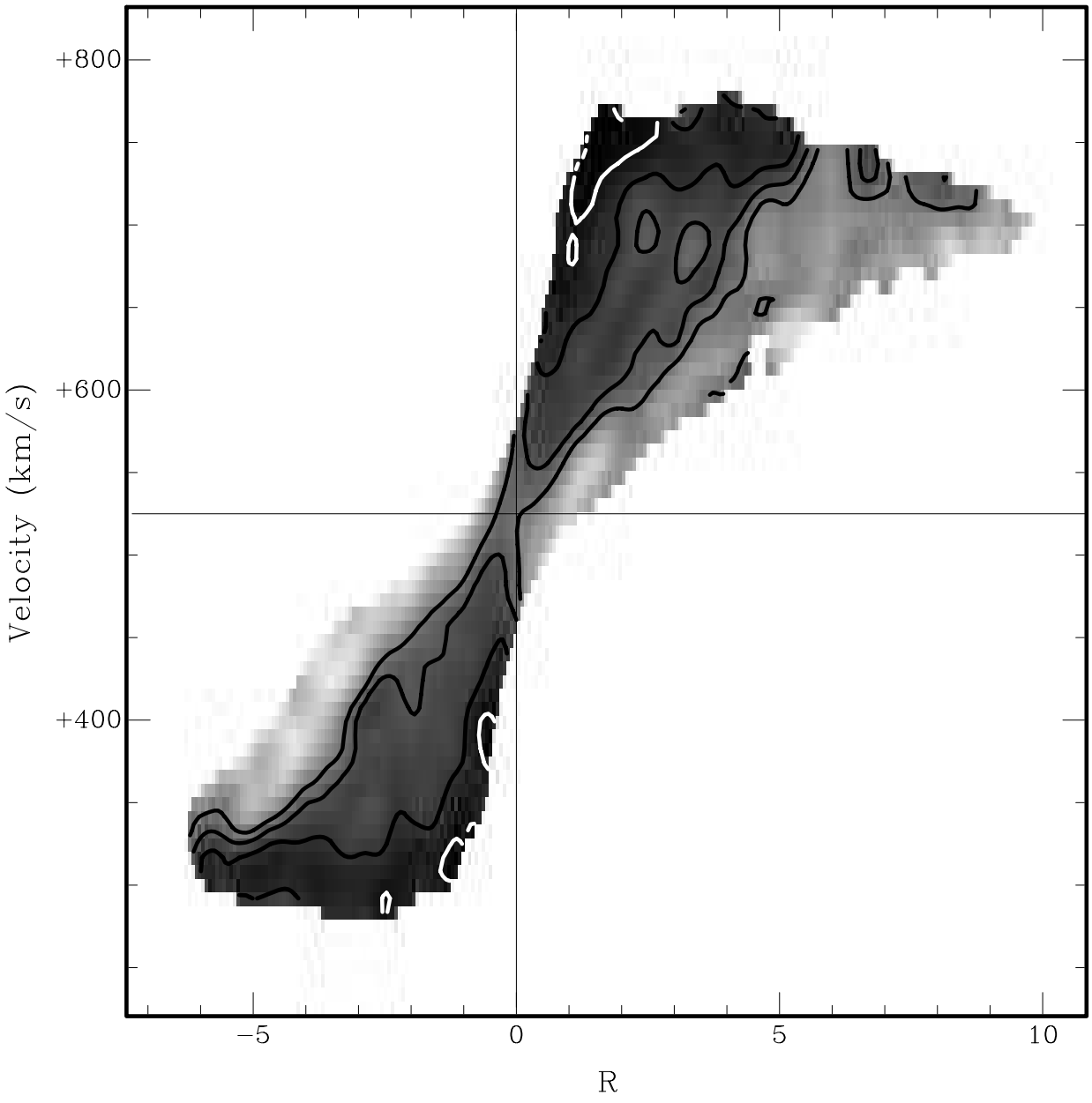

Fig. 6.— Vertical thickness of the H I emission expressed as the first moment of the z distribution at each position in the datacube with respect to the plane of the galaxy. Contour levels are 370 (white), 465, 560 and 650 pc.

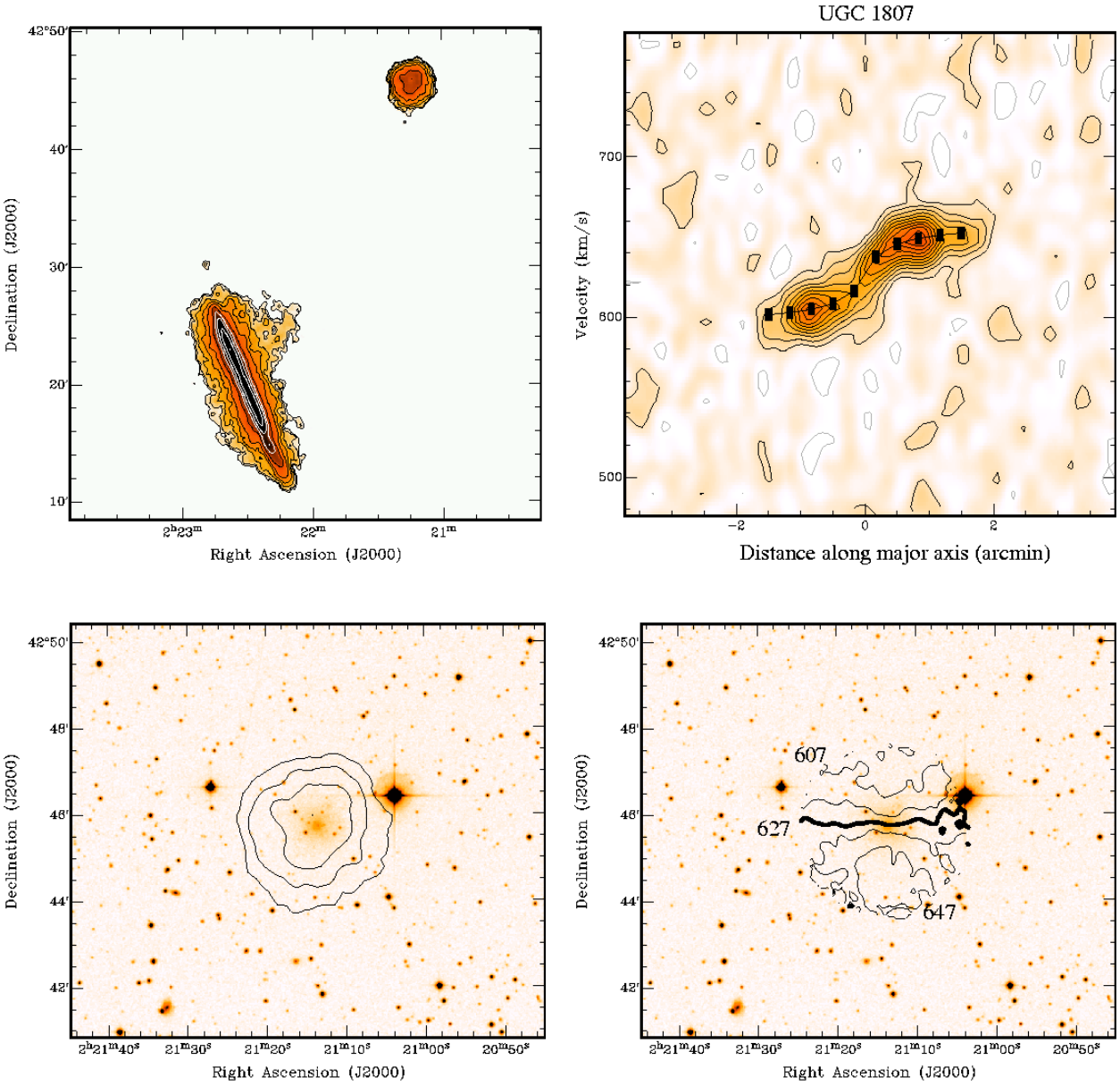

Fig. 7.— Wide field total H I map with NGC 891 and the companion UGC 1807 (top left); Contours showing the total H I emission of the companion, contour levels 1, 2, and 5×10^{20} cm^{-2} (bottom left); velocity field of UGC 1807 (bottom right); p-V plot of UGC 1807 taken along the kinematical major axis, contours 0.135, 0.27 mJy beam^{-1}.

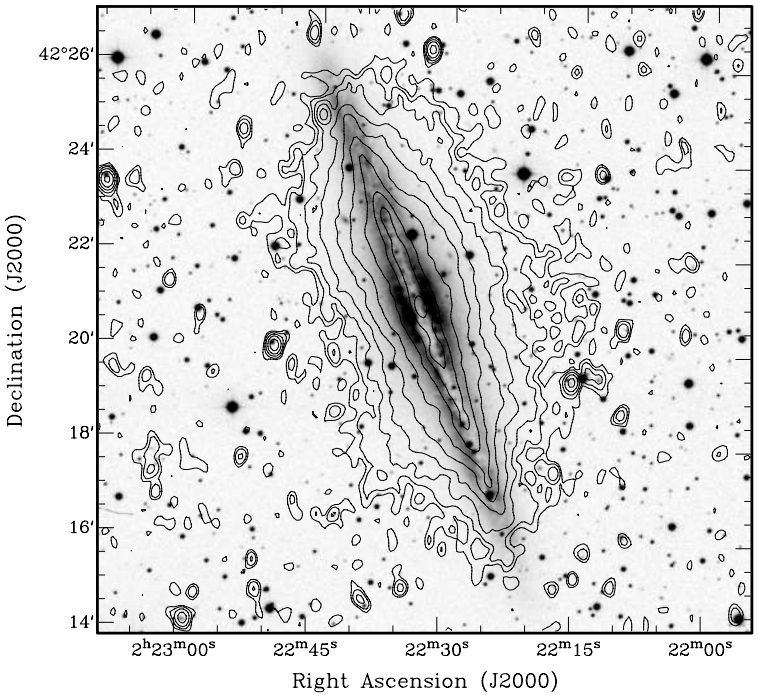

Fig. 8.— Radio continuum contours overlaid on blue optical image taken from the Digitized Sky Survey. Contour levels are 40, 80, 160, 320, ... μJy beam^{-1}.

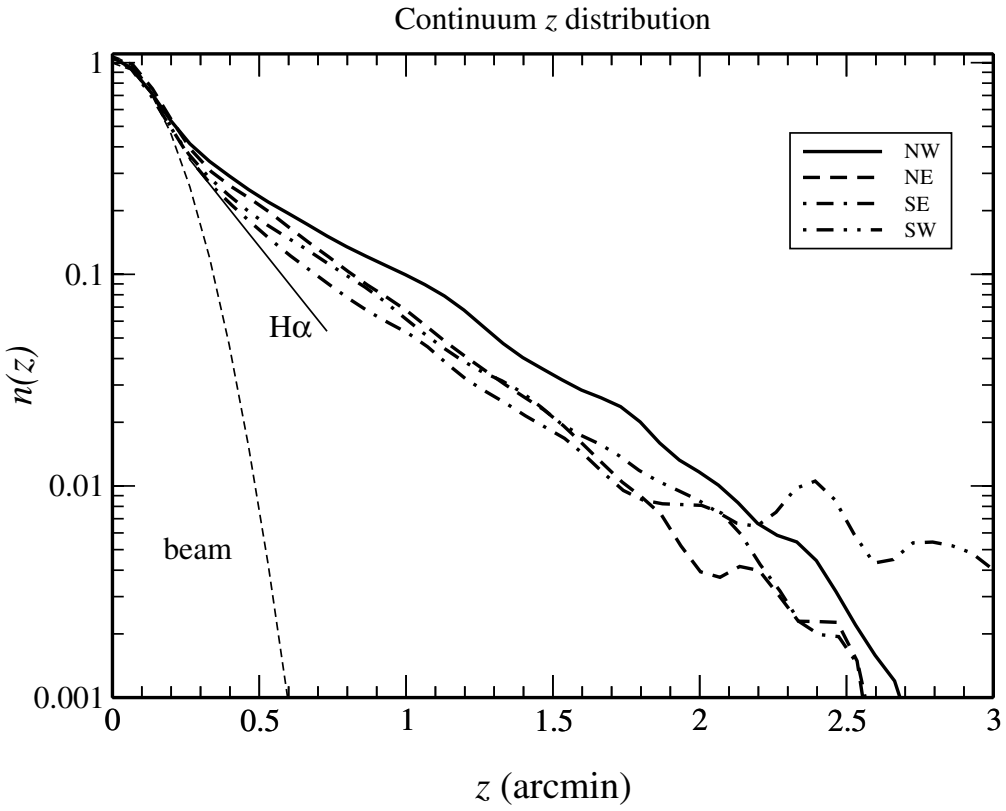

Fig. 9.— Normalised vertical density distributions of the radio continuum halo. The spatial resolution of the observations is indicated. The density distribution of the Hα emission as determined by Rand & Heald (priv. comm.) is indicated.

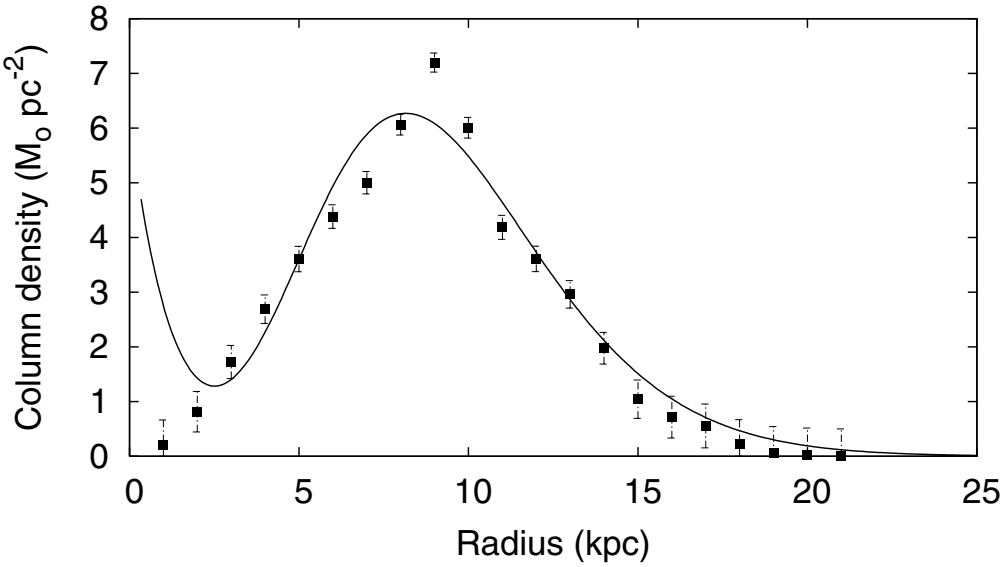

Fig. 10.— H I radial surface density for the thin disk of NGC 891 (squares) overlaid with the fitting formula in eq. 1. In the inner parts a compact exponential component has been added to model the H I ring.

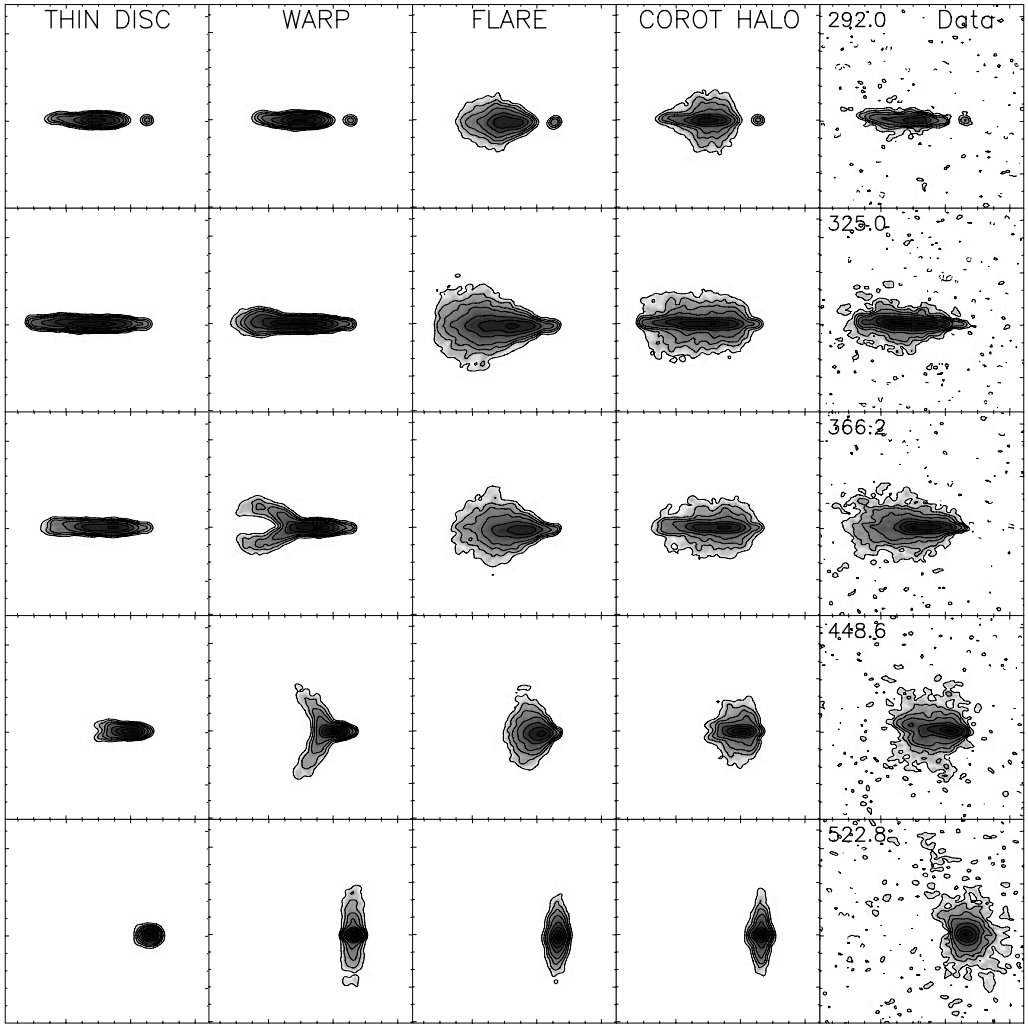

Fig. 11.— Comparison between five representative channel maps for NGC 891 (rightmost column) and models. From left to right the models are: 1) Thin disk; 2) Strong warp along the line of sight; 3) Disk flare; 4) Disk + co-rotating halo. Heliocentric velocities (km sec^{-1}) are shown on top left corners of the data channel maps ($v_{\rm sys} = 528$ km sec^{-1}).

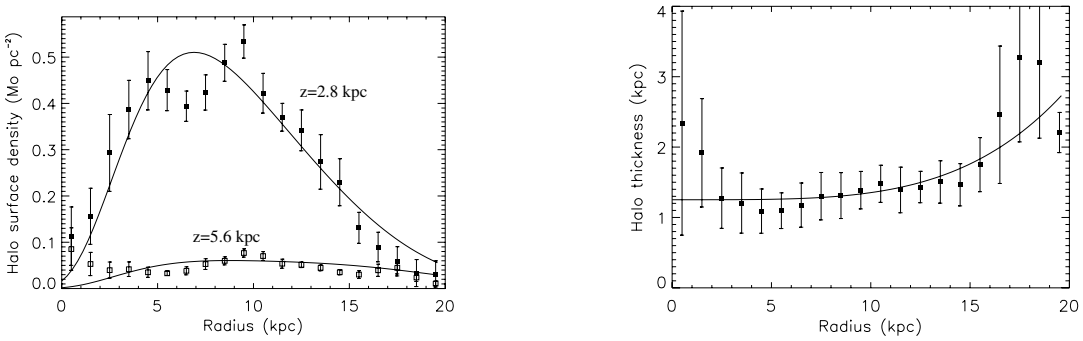

Fig. 12.— Gas distribution in the region of the halo. Left panel: deprojected radial distribution at two distances ($z = 2.8$ and $z = 5.6$ kpc) from the plane (squares). The lines show the results of the fit with eq. 3. Right panel: scaleheight of the gaseous halo $h_{\rm halo}(R)$ (squares) with a power law fit (solid line).

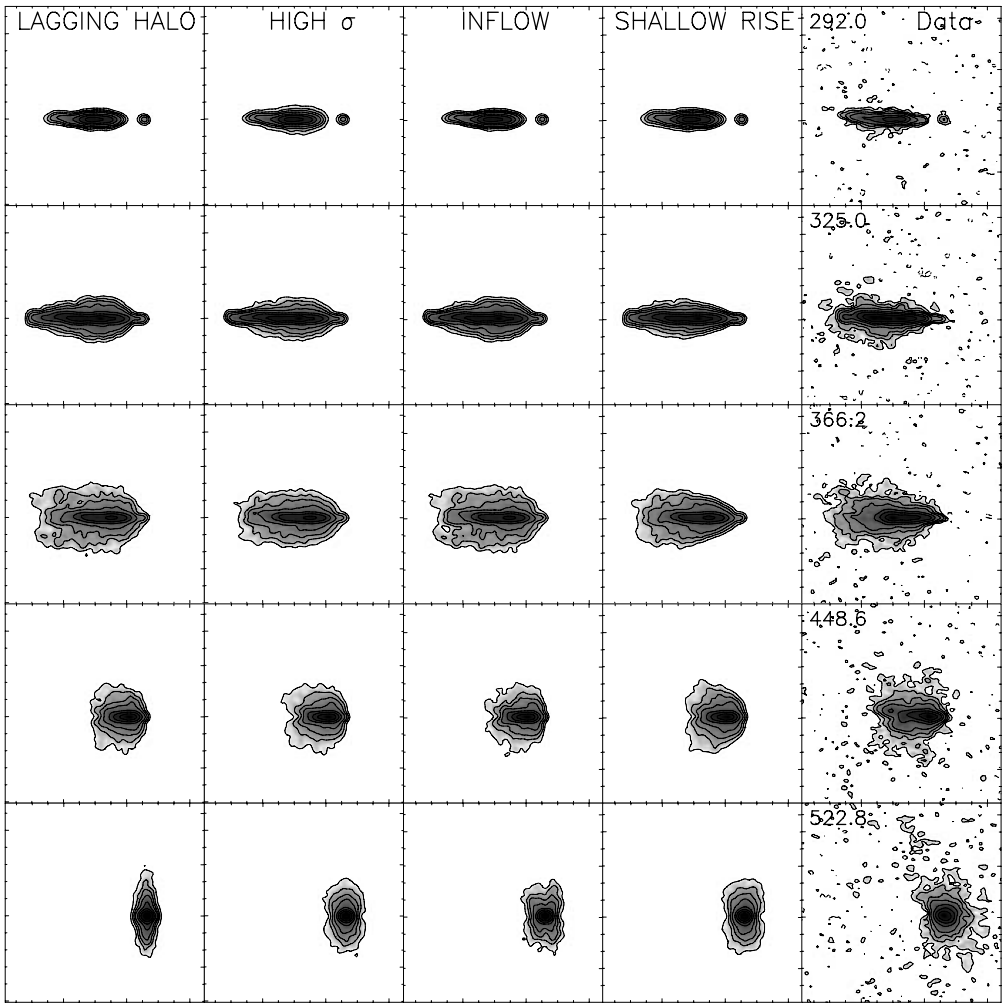

Fig. 13.— Comparison between five representative channel maps for NGC 891 (rightmost column) and models. All the models have a two component (disk+halo) structure with the halo lagging in rotation velocity with respect to the disk. From left to right they are: 1) Lagging halo with constant gradient; 2) Lagging halo with high velocity dispersion; 3) Lagging halo with a radial inflow motion; 4) Lagging halo with velocity gradient increasing in the inner parts. Heliocentric velocities (km sec^{-1}) are shown in the top left corners of the data channel maps ($v_{\rm sys} = 528$ km sec^{-1}).

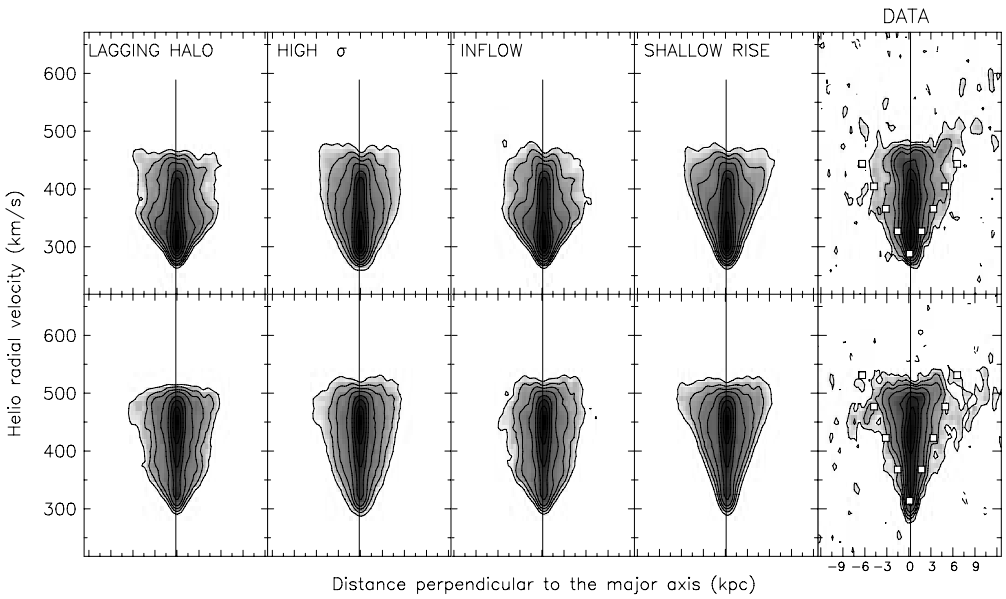

Fig. 14.— Comparison between two position-velocity cuts perpendicular to the plane of NGC 891 (rightmost column) and the models. The top row is taken 2.7′ (7.5 kpc) North of the centre, the bottom row 1.0 ′ (2.8 kpc) The models are the same as in Fig. 13

.

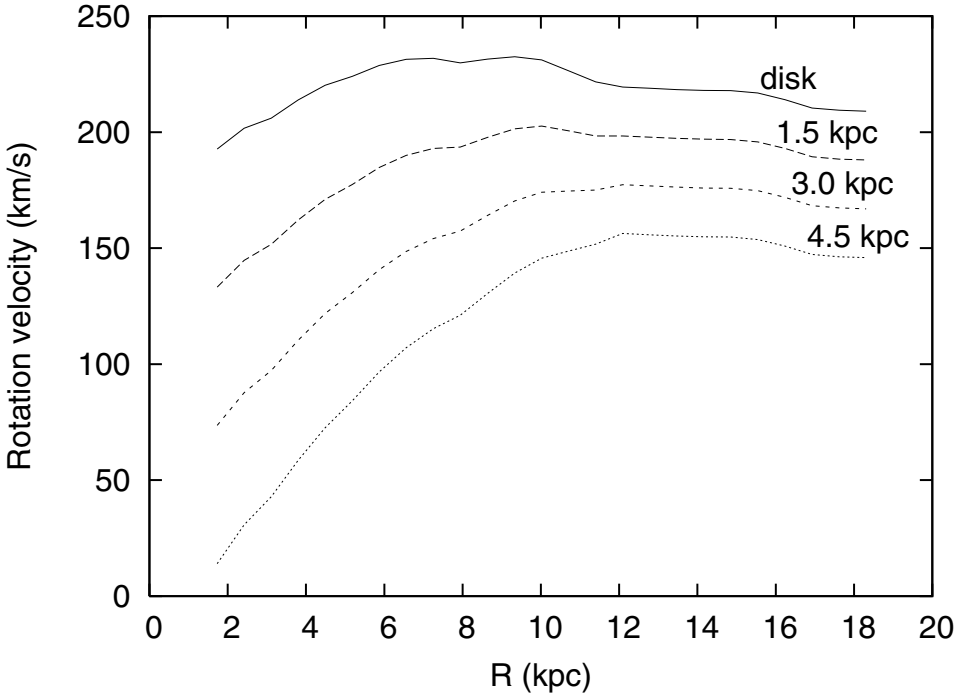

Fig. 15.— Rotation curves as a function of z used in the modelling. In the inner region they become shallower for increasing z-distances from the plane (1.5, 3.0, 4.5 kpc).

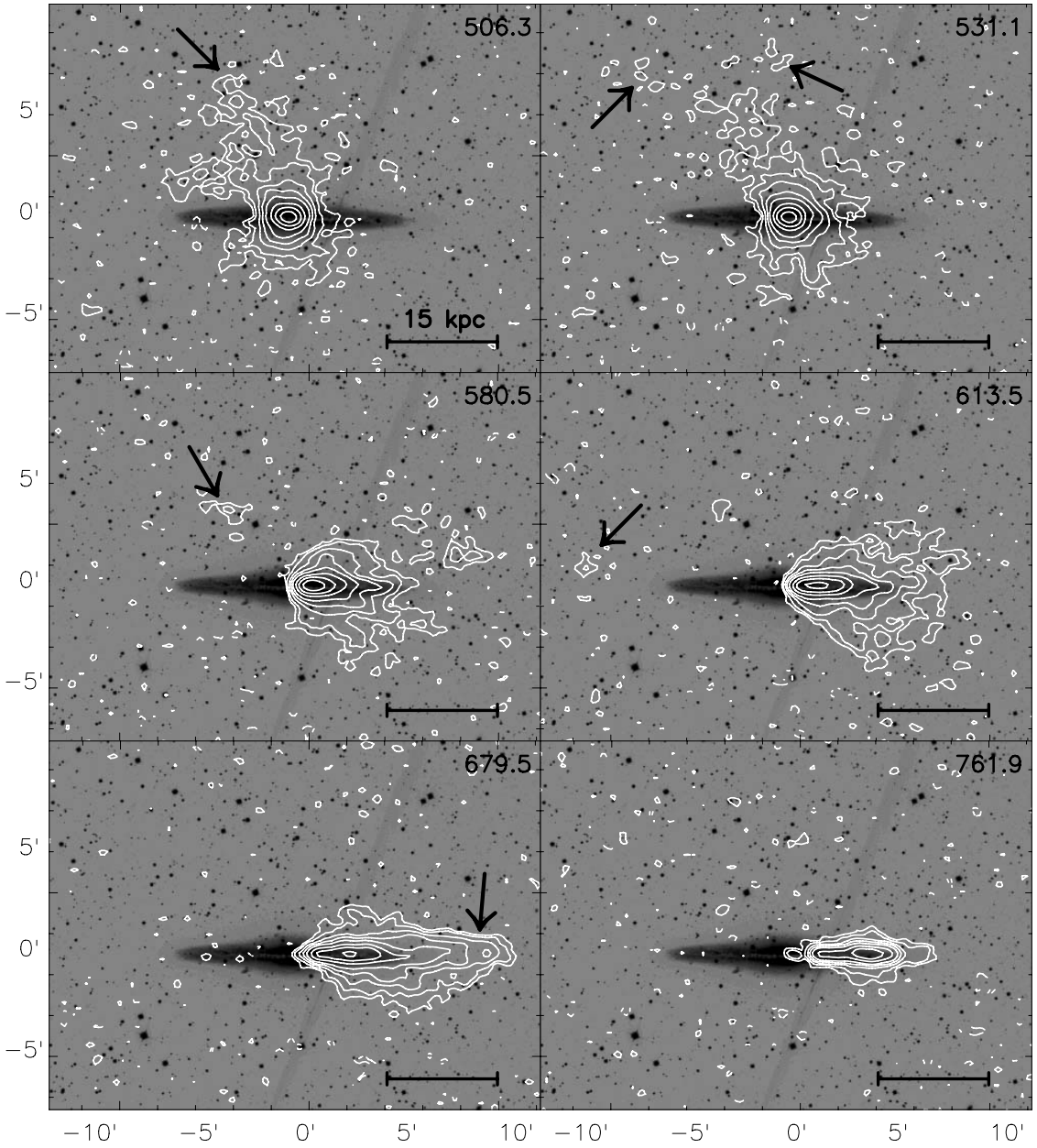

Fig. 16.— Six representative channel maps for NGC 891. The arrows indicate the filament (upper panels), two isolated "counter-rotating" clouds (middle panels), and the extension of the disk in the SW side (lower left panel). The lower right panel shows a channel map at high rotational velocity on the receding side. Note that both the halo gas and the extension in the disk are absent at these velocities. Contour levels are −0.4, −0.18, 0.18, 0.4, 1, 2, 4, 10, 20, 40 mJy/beam.